



HAL
open science

Sulfidation of Ni-bearing goethites to pyrite: The effects of Ni and implications for its migration between iron phases

Zhongkuan Wu, Tingting Zhang, Bruno Lanson, Hui Yin, Dong Cheng, Peng Liu, Feng He

► To cite this version:

Zhongkuan Wu, Tingting Zhang, Bruno Lanson, Hui Yin, Dong Cheng, et al.. Sulfidation of Ni-bearing goethites to pyrite: The effects of Ni and implications for its migration between iron phases. *Geochimica et Cosmochimica Acta*, 2023, 353, pp.158-170. 10.1016/j.gca.2023.06.001 . insu-04235259

HAL Id: insu-04235259

<https://insu.hal.science/insu-04235259v1>

Submitted on 20 Oct 2024

HAL is a multi-disciplinary open access archive for the deposit and dissemination of scientific research documents, whether they are published or not. The documents may come from teaching and research institutions in France or abroad, or from public or private research centers.

L'archive ouverte pluridisciplinaire **HAL**, est destinée au dépôt et à la diffusion de documents scientifiques de niveau recherche, publiés ou non, émanant des établissements d'enseignement et de recherche français ou étrangers, des laboratoires publics ou privés.

1 **Sulfidation of Ni-bearing goethites to pyrite: the effects of Ni**
2 **and implications for its migration between iron phases**

3
4
5 Zhongkuan Wu^a, Tingting Zhang^a, Bruno Lanson^b, Hui Yin^c, Dong
6 Cheng^a, Peng Liu^d, Feng He^{a,e,*}

7
8 ^a*College of Environment, Zhejiang University of Technology, Hangzhou 310014,*
9 *China*

10 ^b*Univ. Grenoble Alpes, Univ. Savoie Mont Blanc, CNRS, IRD, Univ. Gustave Eiffel,*
11 *ISTerre, F-38000 Grenoble, France*

12 ^c*Key Laboratory of Arable Land Conservation (Middle and Lower Reaches of Yangtse*
13 *River), Ministry of Agriculture and Rural Affairs, College of Resources and*
14 *Environment, Huazhong Agricultural University, Wuhan 430070, China*

15 ^d*School of Environmental Studies & State Key Laboratory of Biogeology and*
16 *Environmental Geology, China University of Geosciences, Wuhan 430074, China*

17 ^e*Environment and Civil Engineering, Jiangnan University, Wuxi, Jiangsu, 214122,*
18 *China*

19
20
21
22
23
24
25
26
27
28
29
30 Corresponding author.

31 E-mail address: fenghe@zjut.edu.cn (Feng He).

32

33 **ABSTRACT**

34 Goethite and pyrite are common iron minerals in oxic or anoxic environments,
35 respectively, both minerals being major reservoirs for Nickel, a bio-essential element.
36 Mineral transformation between goethite and pyrite is frequent owing to the alternation
37 of oxic and anoxic conditions in sulfate-rich environments. This mineral transformation
38 has been amply studied, but the effect of Ni on this transformation and its fate along it
39 remain poorly understood. Sulfidation of Ni-free and Ni-containing (through adsorption
40 or isomorphic substitution) goethites was thus studied experimentally by reacting
41 goethite with dissolved S(-II) (molar Fe:S \approx 1:1). X-ray diffraction and associated
42 Rietveld refinement, thermogravimetric analysis, scanning/transmission electron
43 microscopy, X-ray absorption spectroscopy, and wet chemistry were used to monitor
44 mineralogical evolutions and unravel Ni association with reaction products. After 44
45 days of sulfidation, about half of initial goethite converted to iron sulfides:
46 thermodynamically stable pyrite (67%-93%) with minor contents of mackinawite (2%-
47 15%) and greigite (5%-25%). Although the overall content of iron sulfides formed was
48 essentially independent of Ni presence, Ni hampered the conversion from metastable
49 iron sulfides (i.e., mackinawite and greigite) to pyrite (67%-78% vs. 93%, in the
50 presence and absence of Ni, respectively). Pyrite formation from metastable sulfide
51 precursors yielded a uniform Ni distribution in newly formed pyrite, regardless of the
52 initial Ni association with goethite. Although no Ni was released to solution during
53 pyrite formation, Ni incorporation to pyrite results in an increased risk of release to the
54 environment as iron sulfides will be oxidized when exposed to air and water in
55 supergene environments, leading to highly acidic conditions favoring Ni solubility and
56 mobility.

57

58 **Keywords:** Nickel, Goethite, Sulfidation, Iron sulfides, Pyrite, Migration

59

60 **1. Introduction**

61 Laterite (Deoliveira et al., 1992; Dublet et al., 2015; Dublet et al., 2012; Fan and
62 Gerson, 2015; Landers and Gilkes, 2007; Landers et al., 2009) and sulfide deposits
63 (Ikogou et al., 2017; Morin et al., 2017; Noël et al., 2015; Swanner et al., 2019)
64 represent the two most important Ni reservoirs in terrestrial environments (Elias, 2002).
65 In both settings, goethite and pyrite are the two main host minerals for Ni. For example,
66 goethite may present Ni-enrichment up to several weight percents (Dublet et al., 2012;
67 Eliopoulos and Economou-Eliopoulos, 2000; Ugwu and Sherman, 2019) and
68 commonly accounts for ~60-75% of the Ni pool in laterites (Fan and Gerson, 2015;
69 Landers et al., 2009; Manceau et al., 2000). Goethite sequesters Ni, and other transition
70 metals, via surface adsorption (Nachtegaal and Spark, 2002; Ugwu et al., 2019; Xu et
71 al., 2006) and isomorphic substitutions (Cornell, 1991; de Carvalho-E-Silva et al., 2002;
72 Dublet et al., 2015; Landers and Gilkes, 2007; Manceau et al., 2000). Ni(II) adsorbed
73 to goethite surface is commonly considered to readily desorb, whereas incorporation in
74 goethite crystal structure (Ugwu et al., 2019) results in a more stable sequestration. Both
75 adsorbed and structurally incorporated Ni modify goethite's physicochemical properties,
76 affecting its subsequent reactivity, including phase transformation. In particular,
77 adsorbed Ni(II) was reported to compete with other adsorbents for goethite surface sites
78 (Xu et al., 2006) and to delay goethite recrystallization (Friedrich et al., 2019). Ni(II)-
79 for-Fe(III) substitutions also influence vibrational properties of surface hydroxyl groups
80 (de Carvalho-E-Silva et al., 2002), surface charge, or solubility (Ugwu and Sherman,
81 2019) of goethite particles in particular owing to the difference in valence of Fe(III) and
82 Ni(II) in goethite crystal structure (de Carvalho-E-Silva et al., 2002; Friedrich et al.;
83 Gasser et al., 1996; Ugwu and Sherman, 2019; Zachara et al., 2001)

84 Although goethite is the most common and the thermodynamically most stable
85 iron (oxyhydr)oxide on Earth (Cornell and Schwertmann, 2004), it may be altered under
86 reducing conditions through interactions with microorganisms (Maurice et al., 2000;
87 Zachara et al., 2001), organic compounds (Gasser et al., 1996; Larsen and Postma, 2001;
88 Suter et al., 1991), or inorganic reductants (Poulton et al., 2004; Rickard, 1974; Suter

89 [et al., 1991](#)). As a result, goethite may be dissolved ([Dos Santos Afonso and Stumm,](#)
90 [1992](#)) or transformed to secondary Fe minerals such as iron sulfides (e.g. pyrite,
91 mackinawite, etc.) as the result of its interaction with dissolved sulfides [including H₂S,
92 HS⁻, and S(-II), hereafter globally referred to as S(-II)] ([Poulton et al., 2004](#); [Rickard,](#)
93 [1974](#); [Wan et al., 2017](#); [Wang and Morse, 1996](#)). Such reducing conditions are
94 commonly found in flooded sulfate-rich farmlands, wetlands, and marshes, where S(-
95 II) could accumulate up to ~15 mM as the result of microbial anaerobic respiration
96 ([Bagarinao, 1992](#)). A wealth of literature has been devoted to deciphering the
97 interaction of goethite and other iron (oxyhydr)oxides with S(-II), a process commonly
98 referred to as sulfidation ([Kumar et al., 2018](#); [Poulton et al., 2004](#); [Rickard and Luther,](#)
99 [2007](#); [Rickard, 1974](#); [Wan et al., 2017](#)), iron (oxyhydr)oxides being regarded as the
100 main iron suppliers for the early diagenetic formation of pyrite ([Canfield, 1989](#)).
101 Goethite sulfidation is of particular importance as it is regarded as the starting point for
102 sedimentary pyrite formation ([Rickard, 1974](#)), resulting in the association of goethite
103 and pyrite under reducing ([Seyfferth et al., 2020](#)) or alternating oxidizing and reducing
104 conditions ([Otero et al., 2009](#)). Mechanisms of goethite [or other iron (oxyhydr)oxides]
105 sulfidation are well documented: first, S(-II) is adsorbed to the surface of the iron
106 (oxyhydr)oxide allowing an electron-transfer from S(-II) to Fe(III) to form Fe(II),
107 elemental sulfur (S⁰), and polysulfides (S_n²⁻) ([Luther, 1991](#)). S(-II) in excess then
108 precipitates with Fe(II) to form amorphous FeS_x clusters, that transform first to
109 crystalline but metastable monosulfides (mackinawite) and then to greigite. A final
110 reaction between metastable iron sulfides (MIS: mackinawite and greigite) and S⁰, S_n²⁻,
111 or H₂S produces thermodynamically stable pyrite ([de Carvalho-E-Silva et al., 2002](#);
112 [Hurtgen et al., 1999](#); [Lan and Butler, 2014](#); [Luther, 1991](#); [Pyzik and Sommer, 1981](#);
113 [Rickard and Luther, 2007](#); [Schoonen and Barnes, 1991b](#); [Wang and Morse, 1996](#)).

114 In S(-II)-rich sediments, sulfidation of goethite and other Fe (oxyhydr)oxides is a
115 typical process of reductive-dissolution and recrystallization ([Luther, 1991](#); [Wang and](#)
116 [Morse, 1996](#)), and as such strongly influences transport and bioavailability of foreign
117 metals initially associated to goethite ([Hockmann et al., 2020](#); [Zachara et al., 2001](#)).
118 The sole reductive-dissolution of goethite and other iron (oxyhydr)oxides releases both

119 adsorbed [like As and Ni – (Huang et al., 2015; Ren et al., 2018)] and substituted [like
120 Al, Co, Mn, Ni, Cr – (Dubbin and Bullough, 2017; Landers and Gilkes, 2007; Maurice
121 et al., 2000)] foreign elements to aquatic systems. In particular, structurally
122 incorporated Ni(II) may be released to the aqueous phase during a bacteria mediated
123 (Zachara et al., 2001) or HCl caused (Landers and Gilkes, 2007) reductive-dissolution
124 of goethite, or lost during the lateritization process (Dublet et al., 2015). In contrast,
125 when reductive-dissolution occurs in the presence of S(-II), an efficient reducing
126 species (Canfield, 1989; Canfield et al., 1992), this species can readily coprecipitate
127 with both Fe(II) and Ni(II) (Morse and Luther, 1999) thus leading to the formation of
128 solid metal sulfides. Interestingly, the fate of Ni along goethite sulfidation and its effect
129 on this process remain sparingly documented although iron sulfides are also important
130 Ni sinks in sediments (Ikogou et al., 2017; Noël et al., 2015).

131 To bridge this knowledge gap, the present study investigated experimentally the
132 sulfidation of goethite containing adsorbed or isomorphically substituted Ni, to
133 decipher Ni transfer from oxic laterite deposits to anoxic sulfide deposits. Both the
134 mineralogical transformations and Ni retention were characterized using X-ray
135 diffraction, electron microscopy, thermogravimetric analysis, X-ray absorption
136 spectroscopy, and wet chemistry. The main goal of the present work was to elucidate
137 the fate of both adsorbed and substituted Ni(II) species during goethite sulfidation and
138 Ni influence on the process.

139 **2. Experimental Methods**

140 **2.1. Goethite preparation**

141 Ni-free goethite was prepared according to a modified version of Cornell and
142 Schwertmann (2004) protocol. Briefly, 600 mL of a 0.167 M Fe(NO₃)₃ solution was
143 prepared from the dissolution of Fe(NO₃)₃·9H₂O into MilliQ water (18.2 MΩ.cm) in a
144 plastic beaker. Then, 180 mL of 5 M KOH was added in the above solution at a 5
145 mL/min rate with continuous stirring. The obtained suspension was then diluted to 2 L
146 using MilliQ water, and let to settle down and age at room temperature for 7 days. The

147 resulting precipitate was subsequently washed with 400 mL oxalate/ammonium oxalate
 148 solution (pH=3) for 2 hrs to remove amorphous precipitates and adsorbed species, and
 149 dialyzed until conductivity was < 20 μ S/cm. The resulting paste was finally centrifuged,
 150 freeze-dried, ground, and sieved (100 mesh). Ni-incorporated goethites were
 151 synthesized along the same protocol but using mixed $\text{Fe}(\text{NO}_3)_3$ and $\text{Ni}(\text{NO}_3)_2$ solutions
 152 with Ni/(Ni+Fe) molar ratios of 0.02 or 0.06 (Ugwu and Sherman, 2019). Resulting
 153 samples are hereafter referred to as Gt, GtNi2, and GtNi6, according to the initial Ni
 154 contents.

155 Additional Ni-bearing goethite samples were obtained from sorption experiments:
 156 150 mL of a 0.01 M (or 0.04 M) $\text{Ni}(\text{NO}_3)_2$ solution were added to 150 mL of a 10 g/L
 157 Gt suspension, the mixed solution being stirred for 24 hrs. Both Gt suspension and
 158 $\text{Ni}(\text{NO}_3)_2$ solution were prepared using a 0.01 M NaNO_3 ionic background. Before
 159 mixing, the suspension pH was adjusted to 6.00 and allowed to vary by less than ± 0.05
 160 pH units for 12 hrs. The final suspension was centrifuged and washed twice, before
 161 being freeze-dried. Resulting solids are hereafter referred to as GtANi5 (GtANi20).

162 The relative contents of Fe and Ni for Ni-containing goethites were determined by
 163 dissolving 10 mg of solids into 10.00 mL of 6 M HCl solution in duplicates, and metal
 164 concentration was measured via Atomic Absorption Spectroscopy (AAS). Results are
 165 shown in Table 1.

166 Table 1

167 Relative content of Ni and Fe in synthetic goethites.

Samples	c_{Fe} (mg/g)	c_{Ni} (mg/g)	Ni/(Fe+Ni) at. %
GtNi2	572.1 \pm 3.3	6.66 \pm 0.11	1.1
GtNi6	557.1 \pm 1.7	13.26 \pm 0.05	2.2
GtANi5	573.8 \pm 3.5	6.56 \pm 0.05	1.1
GtANi20	566.9 \pm 3.4	9.12 \pm 0.02	1.5

168 2.2 Sulfidation experiments

169 Goethite sulfidation experiments were performed in a glovebox [(Mikrouna, 100%
 170 Ar), maintained at < 1 ppm (v/v) O_2 using a copper catalyst] at room temperature (~ 23
 171 $^\circ\text{C}$) using a protocol similar to that of previous studies (Hockmann et al., 2020; Wan et

172 [al., 2017](#)). Reagents and MilliQ water used in this part were purged with N₂ for more
173 than 4 hrs before being transferred to the glovebox to minimize O₂ content of reacting
174 solutions/suspensions prepared in the glovebox. 1.00 g of Gt, GtNi₂, GtNi₆, GtANi₅,
175 and GtANi₂₀ were then added to 1 L of a 11.24 mmol Na₂S solution (Fe:S molar ratio
176 ≈1), whose pH was adjusted to 6.00±0.10 using HCl and maintained for 12 hrs before
177 goethite addition. Each set was gently stirred with a magnetic stirrer for several mins
178 every day, and the pH was monitored and adjusted manually with HCl or NaOH as
179 needed.

180 At certain time intervals, aliquots were withdrawn for analysis of aqueous and/or
181 solid phases. Aqueous samples were filtered through 0.22 μm nylon membrane (the
182 filtration may be repeated up to 8 times until the solution got colorless due to the
183 formation of colloidal FeS at the beginning of the sulfidation) before further
184 measurement. Ni concentration in solution was determined with AAS, that of Fe(II)
185 with the phenanthroline method ([Fadrus and Malý, 1975](#)), and that of dissolved sulfides
186 via the methylene blue method ([Cline, 1969](#); [Hockmann et al., 2020](#)). Solid samples
187 were retrieved by centrifugation and subsequently dried in the glovebox for several
188 days. They are named as *Sample_name-Reaction_time*; for example, Gt-44d was
189 obtained from Gt reacting with S(-II) for 44 days. Elemental sulfur (S⁰) present on the
190 surface of sulfidized solids was measured using a methanol extraction method: 7.0 mg
191 of solids were added to 7.00 mL of methanol, the mixture being then sonicated for 10
192 mins, and S⁰ content being then determined using high-performance liquid
193 chromatography (Agilent-1260).

194 **2.3 Characterization of goethites and of their sulfidized products**

195 Mineralogy of Ni-free/-bearing goethites, and of their sulfidized counterparts was
196 determined by X-ray diffraction (XRD), using a Bruker D8 Advance diffractometer
197 equipped with a Cu K α source ($\lambda = 1.5418 \text{ \AA}$, voltage 40 kV, current 40 mA), and using
198 a scanning rate of 1 °/min and 0.02 ° step size. Quantitative phase analysis of sulfidized
199 samples was performed through the Rietveld refinement of XRD data using the Profex
200 software ([Döbelin, 2015](#); [Döbelin and Kleeberg, 2015](#)). Thermogravimetric analysis

201 (TGA, Mettler) was performed from room temperature to 800 °C at a heating rate of 10
202 °C/min and under a continuous N₂ flow of 20 mL/min. Scanning electron microscopy
203 (SEM) observations were performed on a Zeiss Sigma300 instrument operated with an
204 accelerating voltage of 30 kV and a working distance of 50 mm. Transmission electron
205 microscopy (TEM) investigations were performed on a FEI Tecnai G2 F30 microscope
206 operated at 300 kV. STEM-HAADF (scanning transmission electron microscopy –
207 high-angle annular dark field) images were obtained using Bruker Super Lite X2.

208 Fe K-edge extended X-ray absorption fine structure (EXAFS) spectra were
209 recorded at the 4B9A beamline of the Beijing Synchrotron Radiation Facility (BSRF).
210 A metallic Fe foil ($E_0=7112$ eV) was systematically used for energy calibration before
211 data collection; data was collected at room temperature and in transmission mode over
212 the 6920-7920 eV range. Data reduction was performed using Athena ([Ravel and](#)
213 [Newville, 2005](#)). Fourier transform (FT) of k^3 -weighted $\chi(k)$ data was performed over
214 the 2.9–12.2 Å⁻¹ k-range to obtain the radial distribution function (RDF) $\chi(r)$ in real
215 space.

216 **2.4 Acid dissolution**

217 From the literature, goethite (α -FeOOH), mackinawite [(Fe,Ni)_{1+x}S], and greigite
218 [Fe(II)Fe(III)₂S₄] are readily soluble in (hot) HCl. Pyrite does not usually dissolve in
219 HCl ([Cooper and Morse, 1998](#); [Cornwell and Morse, 1987](#); [Morse et al., 1987](#)),
220 although nanocrystallinity may allow pyrite dissolution in HCl ([Cooper and Morse,](#)
221 [1998](#); [Cornwell and Morse, 1987](#); [Morse et al., 1987](#)), but is readily dissolved in HNO₃.
222 A HCl-HNO₃ sequential treatment was thus modified from that of [Huerta-Diaz and](#)
223 [Morse \(1990\)](#) to determine the association of Ni with iron oxides/sulfides according to
224 their Fe/Ni release behavior. Specifically, 100 mg of sulfidized samples were added to
225 100 mL of 3 M HCl in a capped conical flask and kept at 40 °C using a water bath.
226 Magnetic stirring could not be used owing to the highly magnetic character of sulfidized
227 solids, and flasks were thus shaken for 5 mins to homogenize the solution every day
228 and before each sampling. After 4 days in HCl, goethite, mackinawite, and greigite
229 were supposed to be fully dissolved, with only pyrite being left. The residual solid was

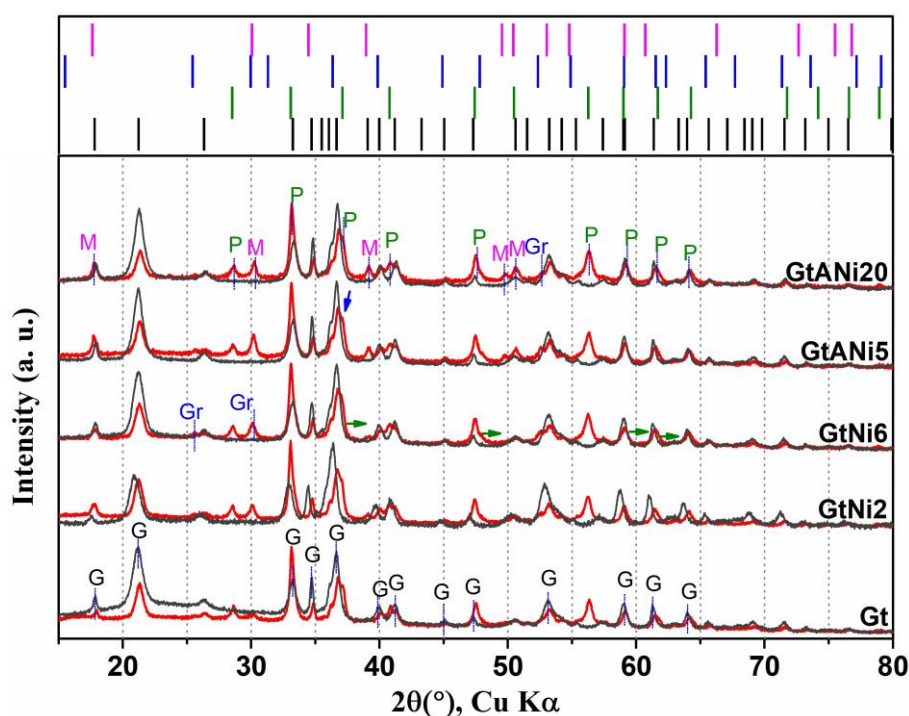
230 then filtered and washed twice, before being transferred in 45 mL of 2 M HNO₃. During
231 both acid treatments, aliquots were sampled at different time intervals to determine Fe
232 and Ni concentrations using AAS. After ~120 hrs of treatment in 2 M HNO₃, solids
233 could still be observed, which could be dissolved completely by adding 10 mL of aqua
234 regia.

235 **3. Results**

236 **3.1. Powder X-ray diffraction**

237 Synthesized Ni-free Gt yielded a diffraction pattern typical for goethite (Fig. 1,
238 ICDD#29-0713). XRD patterns of Ni-bearing goethites were essentially similar to that
239 of Gt, without additional diffraction lines, indicating Ni incorporation in goethite crystal
240 structure or sorption at its surface. After reacting with S(-II) under anoxic conditions
241 for 3 days, XRD patterns of reacted samples were similar to those of their unreacted
242 counterparts, whereas modifications were visible from 7 days of reaction and on (Fig.
243 S1). XRD patterns of Ni-free and Ni-bearing samples were dominated by peaks at
244 ~21.2°/~36.6° (2θ – goethite 110 and 111 reflections – Fig. 1), whereas after sulfidation
245 the peak at ~33.1° (2θ – pyrite 200 reflection) became most intense for all samples.
246 Consistently, intensities of goethite peaks at ~53.3°, ~59.1°, ~61.4°, and ~64.0° (2θ –
247 goethite 221, 151/160, 002, and 061 reflections, respectively) significantly decreased
248 with increasing reaction time. In addition, peaks at ~36.6°, ~47.3°, ~59.1°, and ~61.4°
249 (2θ) shifted to higher angles (green arrows in Fig. 1), and the peak at ~36.6° (2θ) was
250 split on its high-angle side (blue arrow in Fig. 1). These evolutions indicated the
251 formation of new phase(s) at the expense of goethite. Additional reflections at ~28.5°
252 and ~56.3° (2θ) were attributed to pyrite (111 and 311 reflections, respectively -
253 ICDD#42-1340), those at ~30.1°, ~39.0°, and ~49.6° (2θ) to mackinawite (101, 111, and
254 200 reflections, respectively - ICDD#15-0037), whereas weak peaks at ~25.4° and
255 ~52.4° (2θ) indicated the presence of greigite (220 and 440 reflections, respectively -
256 ICDD#16-0713) in reaction products, consistent with previous reports of goethite
257 sulfidation (Wang and Morse, 1996). No nickel sulfides, other iron (oxyhydr)oxides, or

258 elemental sulfur (S^0) were detected using XRD, although the latter was reported in
259 similar studies (Hockmann et al., 2020; Rickard, 1974).

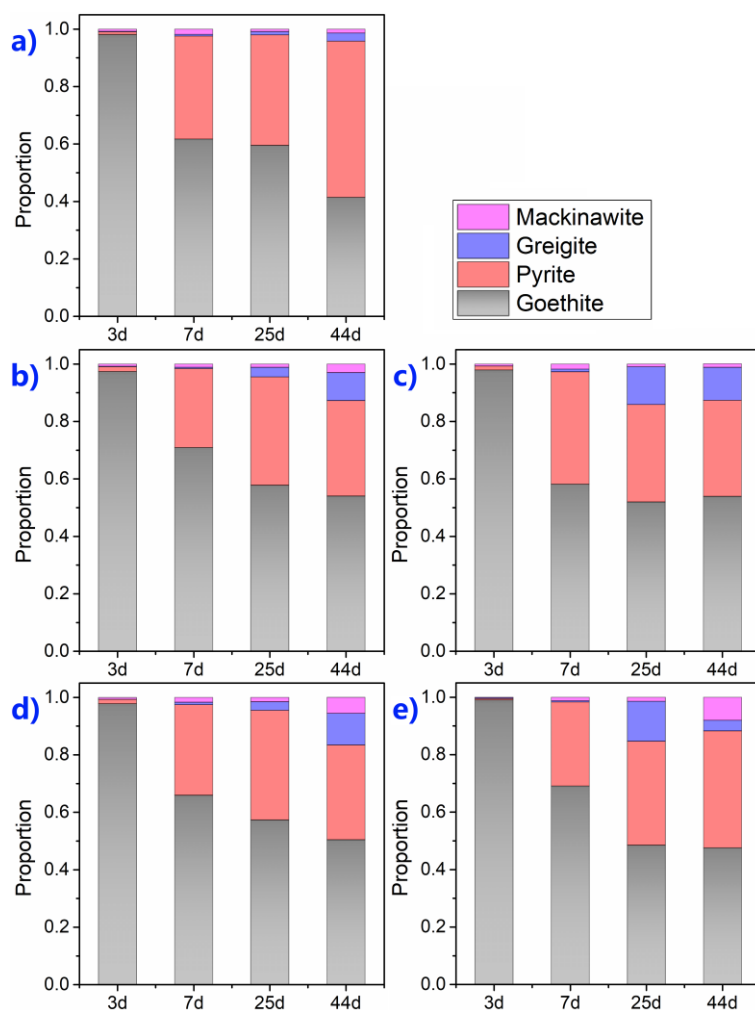


260

261 **Fig. 1** Powder XRD patterns obtained from pristine Ni-free/-containing goethites (black) and from
262 the corresponding reaction products after 44 days of interaction with S(-II) (red). G=goethite,
263 P=pyrite, Gr=greigite, and M=mackinawite. Bars, from bottom to top, above these patterns are
264 characteristic diffraction lines for: goethite (ICDD#29-0713; black), pyrite (ICDD#42-1340; green),
265 greigite (ICDD#16-0713; blue), and mackinawite (ICDD#15-0037; magenta).

266 Quantitative phase analysis was performed using the Rietveld method to quantify
267 the contributions of the four Fe-bearing minerals identified in sulfidized samples (Fig.
268 2, Table S1) in an effort to monitor sulfidation progress. Colloidal FeS and FeS_x clusters
269 remain undetected by this approach however. After 3 days of reaction, minor amounts
270 (~1-2%) of iron sulfide minerals were detected in all runs. After 7 days, ~40% of initial
271 Gt and GtNi6 was converted to iron sulfides, mainly pyrite, that is more than that in
272 GtANi5-7d and GtANi20-7d (~32%), possibly because the pre-existing sorption of
273 Ni(II) to the goethite surface (Hellige et al., 2012; Hockmann et al., 2020; Wan et al.,
274 2017) hindered the interaction of S(-II) with structural Fe(III) during the early stages of
275 GtANi5 and GtANi20 sulfidation, consistent with previous reports (Biber et al., 1994;
276 Poulton et al., 2004). Goethite sulfidation then proceeded, with about half of initial
277 goethite being transformed to sulfides after 44 days of reaction. For example, sulfide

278 content was ~59% in Gt-44d (Table S1), a content significantly higher than that in
 279 sulfidized Ni-bearing goethites (~46-52%, Table S1), suggesting that the association of
 280 Ni incorporated in or adsorbed to goethite significantly hampered its conversion to iron
 281 sulfides. For all samples, pyrite was the main crystalline product of goethite sulfidation
 282 (~33%-54%) (Rickard, 1974), with a minor contribution of greigite (~3%-12%) and
 283 mackinawite (~1%-8%), the latter two being commonly considered as pyrite precursors
 284 (Luther, 1991; Rickard and Luther, 2007). Consistently, the overall content of
 285 metastable iron sulfides (MIS: mackinawite, greigite) remained limited in all reacted
 286 samples, suggesting that pyrite was formed at the expense of MIS or that MIS formation
 287 was inhibited. In addition, MIS appeared less abundant in Gt reaction products
 288 compared to Ni-bearing goethite reaction products.



289

290 **Fig. 2.** Evolution as a function of reaction time of the mineralogy of reaction products of Ni-free/
 291 containing goethites after their interaction with S(-II): a): Gt, b): GtNi2, c): GtNi6, d): GtANi5, and

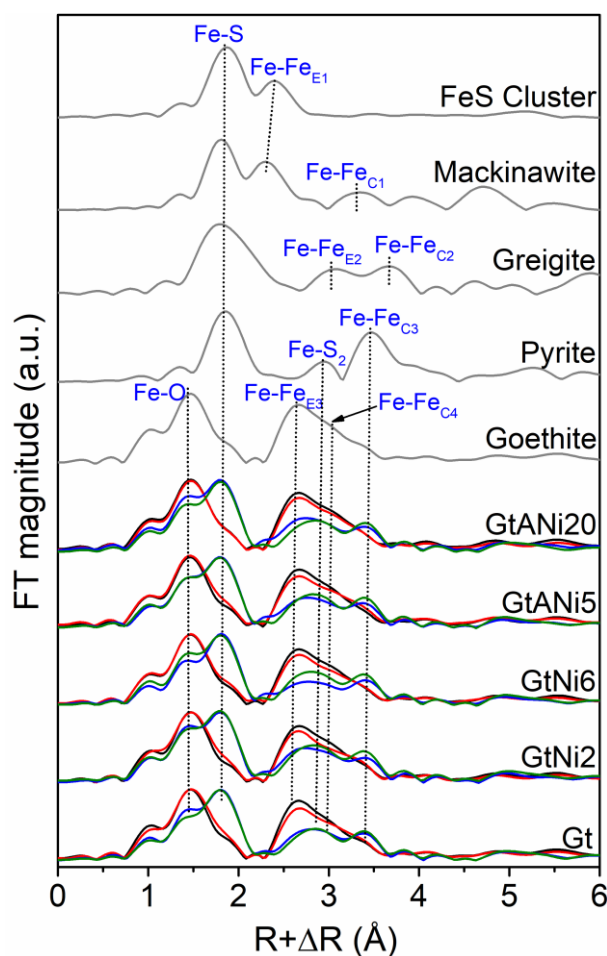
292 e): GtANi20. Errors on mineral fractions are given in [Table S1](#).

293 Incorporation of Ni in goethite led to a minor distortion of its crystal framework,
294 and more especially to a slight expansion of its b unit-cell parameter from 9.957(6) to
295 9.966(8) Å, a and c unit-cell parameters remaining essentially unchanged ([Table S2](#)),
296 consistent with previous reports ([Wells et al., 2006](#)). By contrast, unit-cell parameters
297 of the two Ni-adsorbed samples are logically almost identical to those of Gt. After 44
298 days of sulfidation, the low contents of greigite and mackinawite generate large
299 uncertainties on their unit-cell parameters precluding an unambiguous assessment of
300 their evolution. Unit-cell parameters of pyrite formed both from Ni-free and Ni-bearing
301 goethites are identical within uncertainty.

302 **3.2. Evolution of Fe local environments**

303 Consistent with the above-described mineralogical evolution along goethite
304 sulfidation, Fe local environment was modified as shown by the evolution of Fe K-edge
305 EXAFS spectra ([Fig. S2](#)) and of corresponding RDFs ([Fig. 3](#)). It was not possible to
306 determine relative proportions of the different Fe-bearing phases from linear
307 combination fitting of the EXAFS spectra however. All attempts to fit EXAFS data
308 using reference spectra of colloidal FeS ([Nöel et al., 2020](#)), mackinawite, greigite,
309 pyrite, and goethite did not allow reaching a satisfactory fit (not shown), thus precluding
310 comparison with the mineralogy determined from Rietveld refinement of the XRD data
311 ([Table S1, Fig. S1](#)). The inability to fit the EXAFS signature of the solid fraction is
312 likely related to contrasting signatures of FeS_x clusters present in the solid fraction and
313 of the colloidal FeS reference that was obtained from filtered (<0.02 μm) solutions by
314 [Nöel et al.\(2020\)](#) as suggested by the mismatch between the spectral signature of
315 colloidal FeS and the modification of EXAFS spectra after 3 days of sulfidation ([Figs.](#)
316 [S2 and S3](#)). In both k- and r-space, pristine samples data was typical of goethite ([Burton](#)
317 [et al., 2010](#); [Hohmann et al., 2011](#)), with a first maximum at ~1.50 Å (R+ΔR) in r-space
318 corresponding to the first Fe-O shell and an asymmetric peak spanning from ~2.30 to
319 ~3.60 Å (R+ΔR), peaking at ~2.70 Å (R+ΔR), and corresponding to Fe-Fe bonds in
320 goethite edge- and corner-sharing FeO₆ octahedra. After reacting for 3 days with S(-II),

321 the frequencies of goethite EXAFS spectra in k-space were essentially alike those of
322 pristine samples. Amplitudes were attenuated however (Fig. S2), the modification being
323 most significant for Gt relative to Ni-bearing goethites (Fig. S3), suggesting a negative
324 effect of Ni on goethite sulfidation. Consistently, the Fe-Fe shell at ~ 2.70 Å (R+ΔR) in
325 r-space decreased slightly (Fig. 3), supporting a minor decrease in the number of edge-
326 sharing linkages between FeO₆ octahedra in goethite. In addition, the minor increase of
327 the shoulder at ~ 1.80 Å (R+ΔR) (Fig. 3) supports the early formation of Fe-S bonds,
328 consistent with the formation of FeS_x clusters. After 7-44 days of sulfidation, Fe K-
329 edge spectra were strongly modified compared to that of pristine samples with a major
330 evolution of frequencies in k-space (Figs. S2 and S3). Consistently, the main
331 contribution to the first coordination shell of Fe shifted from ~ 1.50 Å to ~ 1.80 Å
332 (R+ΔR); similarly, the asymmetric peak extending from ~ 2.30 to ~ 3.60 Å (R+ΔR) with
333 a maximum at ~ 2.70 Å (R+ΔR) in pristine samples weakened and split into two isolated
334 peaks of similar intensity at ~ 2.80 Å and ~ 3.40 Å (R+ΔR). The peak at ~ 2.80 Å
335 combines the contributions from edge-sharing Fe-Fe linkages of FeO₆ octahedra in
336 goethite and from Fe-S_{2nd} linkages in pyrite, whereas that at ~ 3.40 Å (R+ΔR) is related
337 to the nearest Fe-Fe shell in pyrite (corner-sharing linkages of FeS_n polyhedra). These
338 modifications are consistent with the conversion of a significant fraction of goethite to
339 iron sulfides after 44 days of sulfidation, most of the conversion occurring from 3 to 7
340 days of sulfidation, consistent with XRD results (Figs. 1, 2, and S1, and Table S1). On
341 the difference plots between reacted and initial samples (Fig. S3), reacted Gt samples
342 systematically showed significantly stronger differences (both after 3 and 44 days of
343 sulfidation), compared to GtNi6 and GtANi20 supporting the negative effect of Ni
344 association to goethite on its sulfidation.



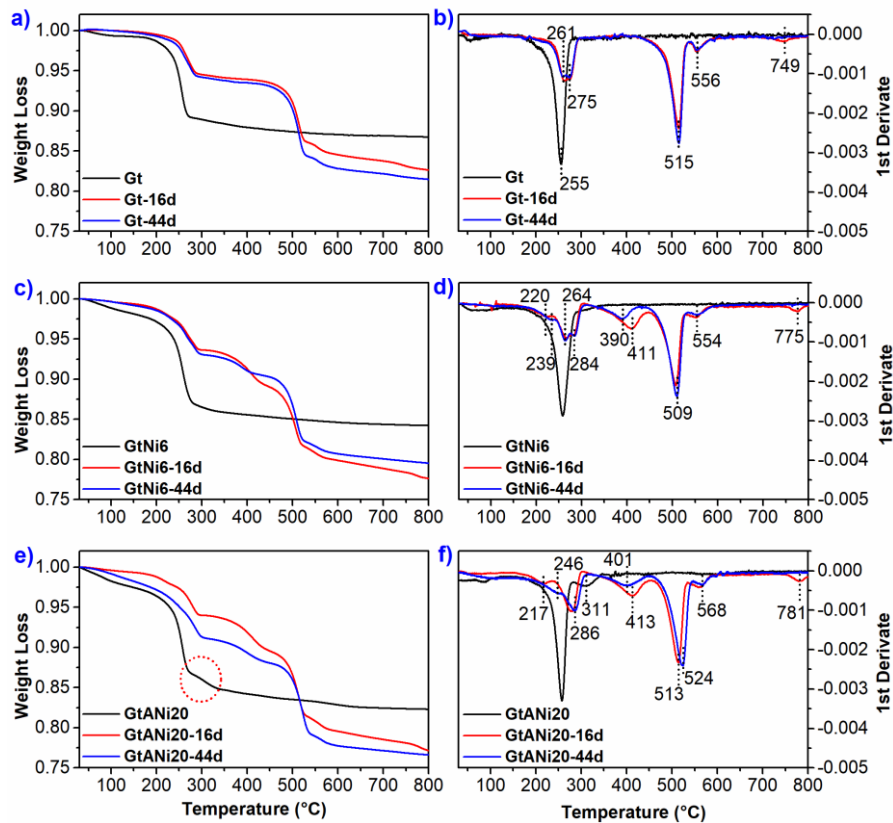
345

346 **Fig. 3.** Fourier transforms of Fe K-edge EXAFS spectra obtained for pristine (black) and sulfidized
 347 goethite samples (red: 3 days, blue: 7 days, green: 44 days), and iron oxyhydroxide/sulfide standards
 348 (gray). To highlight the evolution of Fe local environment, FT intensities were normalized to that of
 349 the first shell. Data for colloidal FeS from Noël et al. (2020). Fourier transform for greigite was
 350 computed from the Fe K-edge EXAFS spectrum calculated with Feff8.4 based on greigite structure
 351 model (COD#9000123 – Ikogou et al., 2017). For mackinawite, Fe-Fe_{E1} and Fe-Fe_{C1} indicate edge-
 352 and corner-sharing linkages of FeS₄-FeS₄ tetrahedra; for greigite, Fe-Fe_{E2} and Fe-Fe_{C2} indicate edge-
 353 and corner-sharing linkages between FeS₆-FeS₆ octahedra and FeS₄/FeS₆-FeS₆ polyhedra,
 354 respectively; for pyrite, Fe-S₂ and Fe-Fe_{C3} indicate the second nearest Fe-S shell and corner-sharing
 355 linkages of FeS₆ octahedra, respectively; for goethite, Fe-Fe_{E3} and Fe-Fe_{C4} indicate edge- and
 356 corner-sharing linkages of FeO₆-FeO₆ octahedra, respectively.

357 3.3. Thermogravimetric analysis

358 Consistent with the observed mineralogical evolution upon goethite sulfidation, the
 359 thermogravimetric analysis of unreacted and reacted samples differed significantly (Fig.
 360 4). All goethite samples (with or without Ni) exhibited a significant weight loss from
 361 ~170 °C to ~300 °C with a maximum at ~255 °C typical for goethite dehydroxylation
 362 and conversion to hematite [α -Fe₂O₃ – (Cornell and Schwertmann, 2004; Ponomar,

363 2018)]. Weight losses occurring prior to dehydroxylation were ascribed to the loss of
364 physisorbed water. An additional weight loss was observed at ~300 °C for GtANi20
365 (Fig. 4e), which is possibly related to the presence of adsorbed Ni(II) on goethite surface.
366 Compared to pristine samples, goethite dehydroxylation weight loss was still observed
367 in sulfidized samples, consistent with the presence of unreacted goethite, but shifted to
368 slightly higher temperature (~270 °C) compared to unreacted samples. In addition, the
369 splitting of TGA data first derivative observed over this low-temperature range (Figs.
370 4b,d) suggests the contribution of another process to the weight loss of sulfidized
371 samples. The temperature shift of goethite dehydroxylation weight loss could
372 correspond to a morphological/size evolution of unreacted goethite whereas the
373 additional process possibly results from the partial conversion of greigite (Krs et al.,
374 1993; Kyprianidou-Leodidou et al., 1997; Sagnotti and Winkler, 1999). For all
375 sulfidized goethites, two major weight losses were observed at ~510-525 °C and ~555-
376 570 °C (Fig. 4) that are typical for pyrite (Yang et al., 2019). Two additional weight
377 losses were observed at low temperatures (~215/220 °C and ~240/245 °C) in sulfidized
378 Ni-containing goethites. These weight losses are possibly related to the presence of Ni-
379 or Ni-rich phases [possibly Ni_{1-x}S – (Bishop et al., 1999)] as they were not observed for
380 sulfidized Ni-free Gt and did not appear to be related to the presence of a specific Fe
381 sulfide species. These Ni-rich phases were not detected using XRD however. Another
382 weight loss was observed at 390/415 °C in the TGA curves of sulfidized Ni-bearing
383 goethites (Figs. 4d,f), but was absent in the reacted Ni-free Gt (Gt-16d/44d). This
384 weight loss is possibly ascribed to the decomposition of NiS_2 to NiS (Dunn and Kelly,
385 1977).



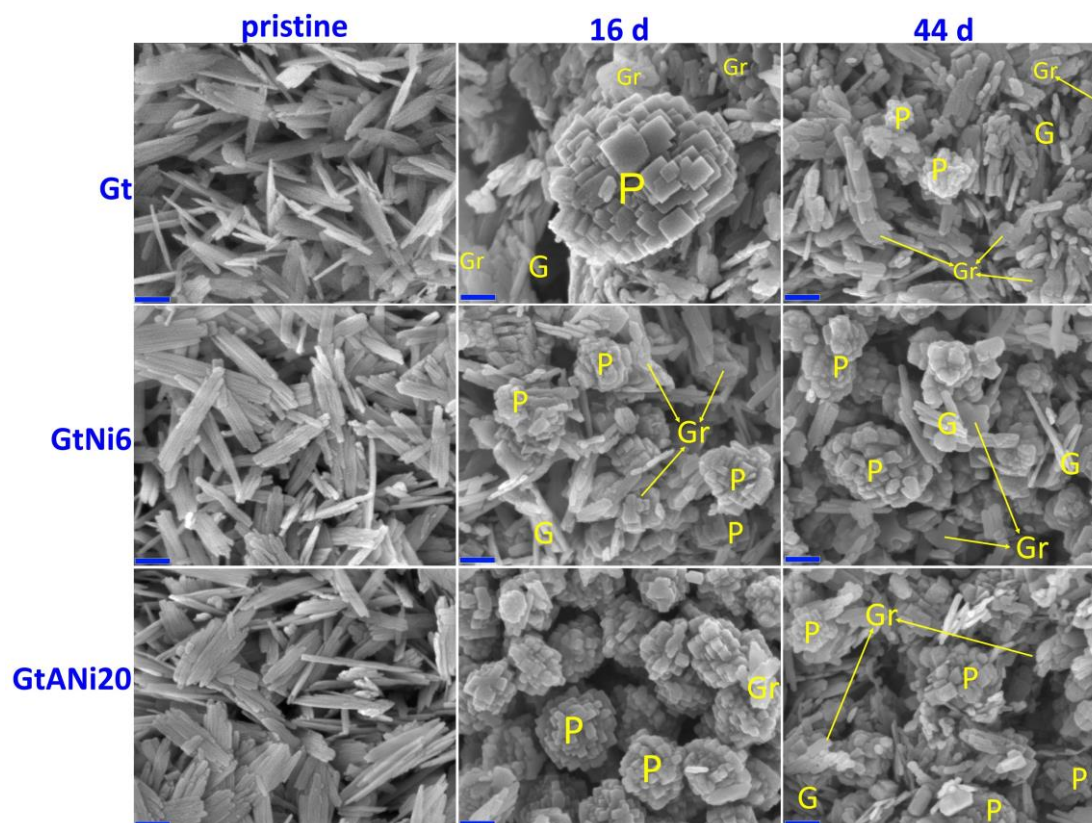
386

387 **Fig. 4.** Experimental thermogravimetric curves (left) and their first derivatives (right) for pristine
 388 (black) and sulfidized goethite samples (red: 16 days, blue: 44 days): a,b) Gt; c,d): GtNi6; e,f)
 389 GtANI20.

390 3.4. Electron microscopy

391 Goethite sulfidation and the associated crystallization of Fe-rich sulfides (pyrite,
 392 greigite, mackinawite) were associated with a dramatic morphological evolution (Figs.
 393 5 and S4). All pristine goethite samples were acicular shaped with lath lengths ranging
 394 ~300-400 nm or more, typical for goethite (Cornell and Schwertmann, 2004), and no
 395 significant difference was detected between Gt and Ni-bearing samples. Crystal habits
 396 were more heterogeneous in sulfidized samples with three main crystal habits: i) laths
 397 extending ~100-300 nm in length and corresponding to residual goethite after their
 398 interaction with S(-II); ii) framboids extending several hundred nanometers in diameter
 399 and composed of cubic pyrite nanocrystals (Wang and Morse, 1996); iii) irregular
 400 lamellas, possibly corresponding to greigite as suggested by lattice fringes exhibiting
 401 ~0.350 and 0.285 nm periodicities [greigite (220) and (222) planes; Fig. S4f,i – (Cao et
 402 al., 2009; Islam and Patel, 2017; Lan and Butler, 2014)]. Although Rietveld refinement

403 indicated that half of the initial goethite was preserved in sulfidized samples (Table S1),
404 the framboids and irregular lamellas visually dominated the three sulfidized samples,
405 suggesting that residual goethite might be covered by newly formed iron sulfides.
406 Contrasting with micrometer-sized cubic/polyhedral pyrite crystals reported previously
407 (Butler and Rickard, 2000; Du et al., 2021; Liu et al., 2022; Lowers et al., 2007), pyrite
408 grain sizes ranged from tens to hundreds of nanometers in the present sulfidized
409 goethites. Consistent with previous TEM observations (Kumar et al., 2018; Peiffer et
410 al., 2015), no joints between pyrite framboids and goethite laths were observed, thus
411 confirming that the goethite-to-iron sulfides transformation proceeded mainly through
412 dissolution-recrystallization (Wang and Morse, 1996), rather than as a solid-state
413 conversion.

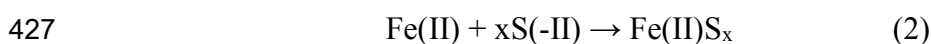


414
415 **Fig. 5.** Scanning electron micrographs of pristine and sulfidized Ni-free/-bearing goethites. G, P, Gr,
416 and M stand for goethite, pyrite, greigite, and mackinawite, respectively. Blue scale bars at the lower
417 left of each figure represent 100 nm.

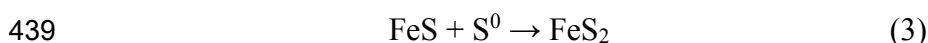
418 **3.5. Solution chemistry during sulfidation (S(-II) and Fe(II)**

419 **concentrations)**

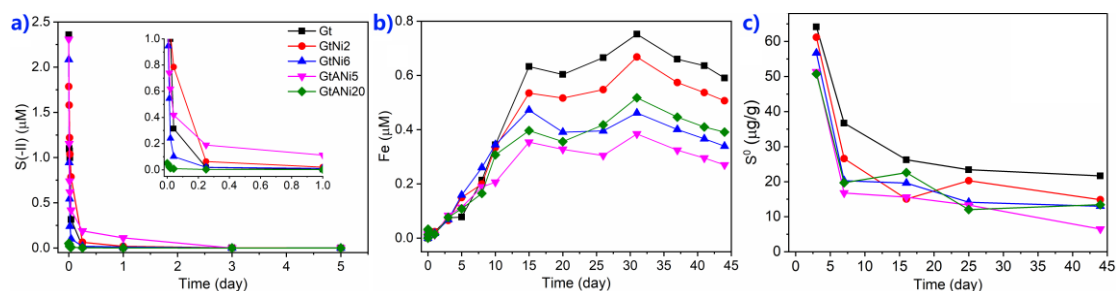
420 S(-II) concentration in solution decreased dramatically below the detection limit of
 421 the methylene blue method (0.02 mg/L) within 3 days (Fig. 6a). S(-II) consumption rate
 422 was similar for all goethite samples. This decrease resulted from the quick adsorption
 423 of S(-II) to goethite surface and from the subsequent swift formation of amorphous FeS_x
 424 clusters induced by S(-II) interactions with Fe(II) (Poulton, 2003; Wan et al., 2017)
 425 according to:



428 Consistently, Fe(II) and elemental sulfur (S⁰) were produced as the result of these
 429 interactions immediately after adding goethite to the S(-II) solution (Figs. 6b,c). After
 430 an initial steady increase, Fe(II) content in solution stabilized after ~15 days of
 431 sulfidation, most likely because Fe(II) consumption related to Fe sulfides formation
 432 compensated its production according to Eq. 1, and to the subsequent destabilization of
 433 both FeS_x clusters / colloidal FeS and MIS. After a possible sharp initial increase (not
 434 detected), S⁰ amount decreased gradually in the system most likely as the result of pyrite
 435 formation from Fe sulfide precursors according to Eq. 3 (Rickard, 1975). Consistent
 436 with quantitative phase analysis, pyrite formation was most noticeable over 3-7 days in
 437 all experiments (Table S1, Fig. 6c). Ni concentration in solution was systematically
 438 lower than its detection limit with AAS (0.05 mg/L – data not shown).



440



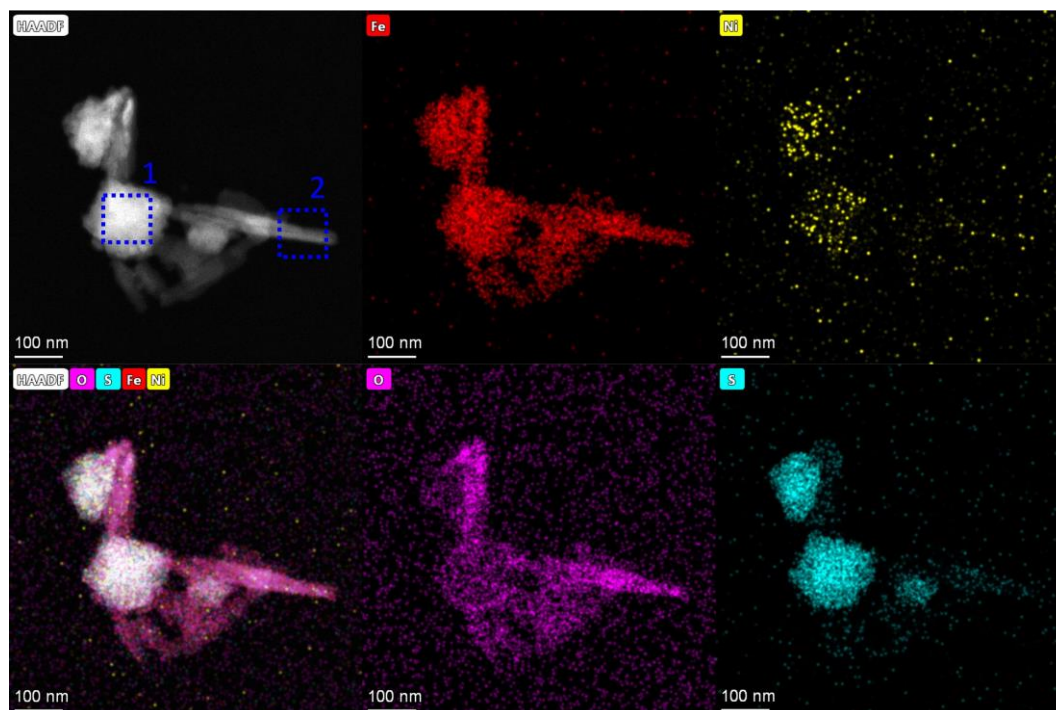
441

442 **Fig. 6.** Evolution of (a) S(-II) and (b) Fe(II) concentration in solution and (c) relative mass of

443 elemental sulfur (S^0) associated with the solids as a function of sulfidation time for Ni-free/-bearing
444 goethites. S^0 content was quantified only for sulfidized samples.

445 3.6. Solid chemistry during sulfidation

446 Content and distribution of Fe, Ni, O, and S within sulfidized particles were
447 determined using HAADF imaging coupled with EDX analysis (Figs. 7 and S5).
448 Fibrous morphologies were ascribed to goethite crystals, whereas bright areas in
449 HAADF dark field micrograph were mainly related to aggregated crystals shown in
450 Figs. 5 and S5 and identified as iron sulfides, consistent with elemental distributions.
451 Both Fe and O were evenly distributed in both types of crystals however, consistent
452 with the formation of Fe sulfides on residual goethite particles. On the other hand, Ni
453 and S appeared to be concentrated in the bright areas, the distributions of the two
454 elements being highly correlated, indicative of the slight Ni enrichment of newly
455 formed iron sulfides compared to residual goethite. For example, Ni mass fraction in
456 selected Fe sulfide polycrystals and goethite crystals (areas #1 and #2, respectively, in
457 Fig. 7 upper left) were $0.9 \pm 0.3\%$, and $0.5 \pm 0.2\%$, respectively.



458

459 **Fig. 7.** STEM/HAADF micrograph (upper left) and EDX maps for Fe (upper center), Ni (upper
460 right), O (lower center), S (lower right), and composite Fe-Ni-S-O image obtained for GtANi20-
461 44d.

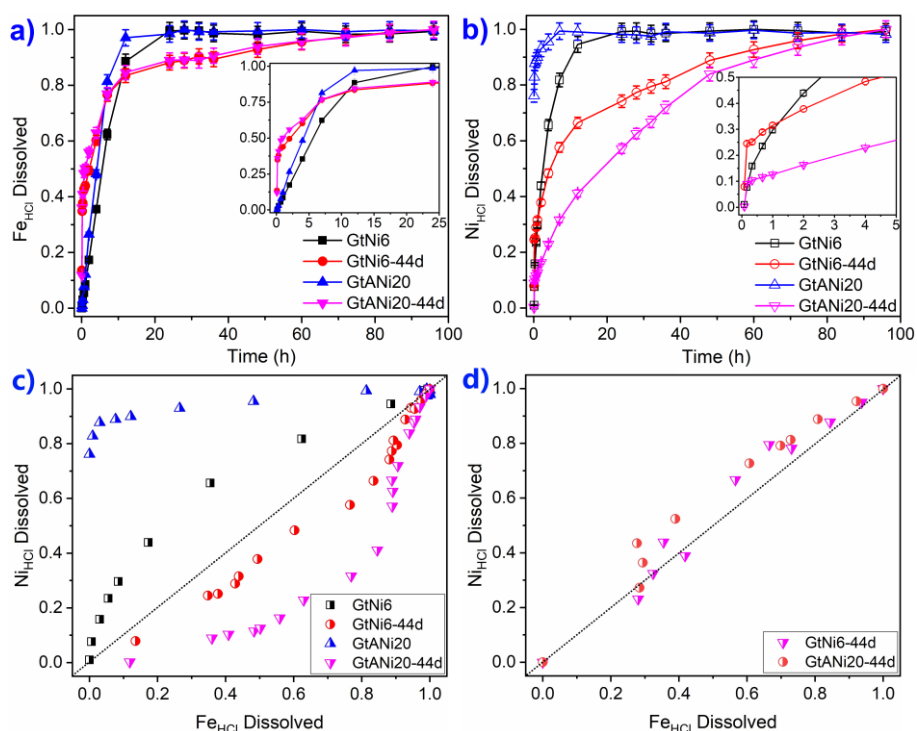
462 3.7. Acid Treatment of pristine and sulfidized samples

463 3.7.1 HCl treatment and kinetic modeling

464 Fe was steadily released from pristine GtNi6 and GtANi20 upon 3 M HCl treatment
465 and Fe concentration in solution reached a plateau after ~24 hrs (Fig. 8a), even though
466 the former dissolved slightly slower than the latter (inset in Fig. 8a). By contrast, Fe
467 release from their sulfidized counterparts appeared more complex. The initial (~10 mins)
468 Fe release from sulfidized samples is larger than that of their pristine equivalents (inset
469 in Fig. 8a), likely as the result of Fe(II) desorption from mineral surfaces and from the
470 dissolution of FeS_x clusters and MIS. Following this initial fast stage, Fe release from
471 sulfidized samples slowed down from 10 mins to ~12-24 hrs, a period during which
472 goethite dissolution is the main process releasing Fe to solution. In contrast to pristine
473 goethite samples that were thoroughly dissolved after 24 hrs of hydrochloric acid
474 treatment, Fe release from sulfidized samples continued, most likely owing to
475 dissolution of nanocrystalline pyrite at this stage, consistent with the enhanced
476 solubility of fine-grained pyrite in HCl (Cornwell and Morse, 1987). Dissolution of
477 fine-grained pyrite is supported by the overall Fe release during HCl treatment that
478 exceeds the relative proportion of goethite and crystalline MIS determined by XRD in
479 sulfidized samples (~60-67 wt% – Table S1, Fig. S6). These proportions do not account
480 for FeS_x clusters. Fe release rate was significantly decreased however, and no plateau
481 was reached during the HCl treatment of sulfidized samples, even after 96 hrs.

482 The release of Ni associated to pristine goethite and to corresponding sulfidized
483 samples differed significantly from that of Fe in these phases but also from one sample
484 to the other (Fig. 8b). For example, Ni in GtNi6 was released slightly faster than Fe,
485 both metals reaching a maximum concentration after ~24 hrs and complete goethite
486 dissolution. In contrast, most adsorbed Ni present in GtANi20 was quickly released to
487 the solution (~76% after 5 mins of the HCl acidic treatment) before reaching a plateau
488 after ~7 hrs. Their sulfidized counterparts (GtNi6-44d and GtANi20-44d) exhibited
489 contrasting Ni release rates before and after ~10 mins of interaction with HCl (inset in
490 Fig. 8b), consistent with Fe release. In particular, ~25% and ~9% of Ni was released

491 from GtNi6-44d and GtANi20-44d, respectively, within the first 10 mins of interaction.
 492 After this initial fast release, which likely represents Ni associated to FeS_x clusters and
 493 MIS, Ni release from both samples appeared steady with no obvious rate modification.
 494



495 **Fig. 8.** Kinetic release of (a) Fe and (b) Ni during HCl treatment of pristine GtNi6 and GtANi20 and
 496 of their sulfidized counterparts. (c) Congruency of Ni versus Fe release during HCl treatment of
 497 pristine GtNi6 and GtANi20 and of their sulfidized counterparts during the whole treatment. (d)
 498 Congruency of Ni versus Fe release during HCl treatment of sulfidized samples (GtNi6-44d and
 499 GtANi20-44d) excluding data points before 24hrs. The $y=x$ line is plotted as a dotted line in (c) and
 500 (d).
 501

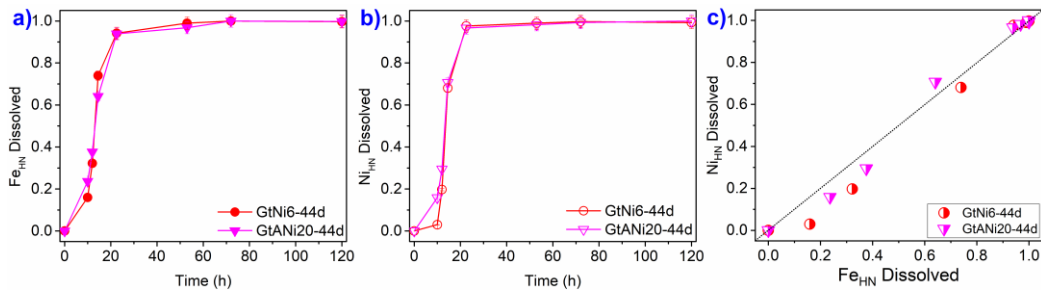
502 Simulations of Fe and Ni release kinetics during HCl treatment were performed
 503 using one-phase exponential decay function to evaluate the relative release of the two
 504 metals from pristine and sulfidized samples (Fig. S7, S8, and Table S3). The rates (1st
 505 derivative of kinetics) of Fe and Ni released from all the examined samples decreased
 506 as a function of time, and the relative release rate of Ni to Fe varied gradually (Fig. S7).
 507 For GtANi20, the adsorbed Ni experienced fast release while structural Fe was released
 508 gradually, producing an inverted-L relative release curve of Ni to Fe (Fig. 8c). For
 509 GtNi6, Ni (~69%) was released faster compared to Fe (~44%) before ~4.30 hrs and
 510 slower after that, yielding a convex relative release curve (Figs. 8c and S7), indicating

511 a non-uniform distribution of Ni in goethite (Girgin et al., 2011; Landers and Gilkes,
512 2007; Landers et al., 2009), with a significant Ni-enrichment in goethite outer layers.
513 For sulfidized samples, Fe was released slightly or significantly faster relative to Ni
514 upon the HCl treatment, and the rates dropped until equal to each other at ~9.60 hrs and
515 ~7.10 hrs for GtNi6-44d and GtANi20-44d, respectively (Figs. 8c and S7). Although
516 both sulfidized samples displayed rather similar trends of Fe release (~76% vs. ~78%
517 after 7.70 hrs), Ni was released faster from GtNi6-44d than from GtANi20-44d before
518 ~7.70 hrs (~60% vs. ~33%, Fig. S8). Interestingly, both sulfidized samples led to a
519 concave relative release curve (Fig. 8c), that of GtNi6-44d being close to the $y=x$ line.
520 In contrast, that of GtANi20-44d was far from the line, indicating that Ni was more
521 homogeneously distributed in GtNi6-44d compared to that in GtANi20-44d. In addition,
522 GtANi20-44d most likely contained more Ni-free/poor phase(s) (residual goethite
523 mainly) that were readily extracted by HCl and Ni-rich cores. The two sulfidized
524 samples contained multiple Fe species [i.e., adsorbed Fe(II), goethite, FeS_x clusters,
525 greigite, mackinawite, and pyrite], each likely releasing Fe at a different rate, especially
526 during the first ~24 hrs of the treatment. To overcome this issue, the relative release
527 curve was plotted excluding data points measured during this initial 24 hrs period (Fig.
528 8d). This curve was close to the $y=x$ line, indicating Ni was homogeneously distributed
529 in nanocrystalline pyrite.

530 3.7.2 HNO_3 treatment

531 When sulfidized samples pre-treated with HCl were equilibrated in 2 M HNO_3 , the
532 release of Fe and Ni proceeded (Fig. 9), accounting for the sole pyrite dissolution. For
533 both GtNi6-44d and GtANi20-44d, Fe release rate was significantly enhanced by HNO_3
534 treatment, and reached plateaus after ~48-72 hrs. Ni release was strongly correlated to
535 that of Fe, leading to an almost linear relative release curve (Fig. 9c), indicative of a
536 homogeneous Ni distribution in pyrite crystals.

537



538

539 **Fig. 9.** Kinetic release of (a) Fe and (b) Ni during HNO₃ treatment of HCl-treated sulfidized GtNi6-
 540 44d and GtANI20-44d. (c) Congruency of Ni versus Fe release during HNO₃ treatment of HCl-
 541 treated sulfidized GtNi6-44d and GtANI20-44d. The y=x line is plotted as a dotted line in (c).

542 4. Discussion

543 4.1 Mineralogical evolution along goethite sulfidation

544 In the present study, diffraction (Figs. 1 and S1), electron microscopy (Figs. 5 and
 545 S5), and spectroscopic (Figs. 3, S2, and S3) data consistently show that crystalline
 546 products of goethite sulfidation consist mainly of pyrite with minor mackinawite and
 547 greigite. Sulfidation of goethite and other iron (oxyhydr)oxides thus appears as a
 548 pathway possibly accounting for the coexistence of iron (oxyhydr)oxides and of these
 549 iron sulfides in natural anoxic or alternating oxic-anoxic sediments and soils (Kalatha
 550 and Economou-Eliopoulos, 2015; Otero et al., 2009; Seyfferth et al., 2020). In nature,
 551 goethite and iron monosulfide (FeS) prevail in surface or subsurface horizons of soil
 552 profiles, whereas pyrite is the major iron-bearing mineral in deep horizons (Kraal et al.,
 553 2013; Seyfferth et al., 2020). Experimental studies, including the present one, provide
 554 additional insights into specific conditions favoring the formation of one phase or the
 555 other, common iron sulfides obtained from goethite sulfidation being amorphous FeS_x
 556 clusters, mackinawite, greigite, and pyrite (Table 2). More especially, solution pH,
 557 relative abundance of goethite [(Fe(III))] and dissolved sulfides [S(-II)], and reaction
 558 duration appear to be responsible for reaction product diversity.

559 Table 2

560 Conditions of goethite reaction with S(-II) and mineralogy of iron sulfides reported in the literature
 561 and in the present study

c _{Fe}	c _{S(-II)}	Fe:S	pH	Reaction Duration	Products	Identification Methods	References
11.20	50.00	0.22	7.77	~2 hrs		XRD	Rickard, 1974
11.20	100.00	0.11	7.64				

11.20	200.00	0.06	7.50		amorphous		
11.20	400.00	0.03	7.24		FeS _x ,		
11.20	500.00	0.02	6.95		mackinawite		
1.12	4.50	0.25	7.55				
5.10	4.16	1.23	7.61				
1.04	4.90	0.21	7.54	~24 hrs	iron monosulfide	chemical method	Pyzik and Sommer, 1981
3.17	2.60	1.22	7.54				
1.06	5.50	0.19	7.42				
1.06	5.40	0.20	7.40				
n.i.	17.40		5.12	~2160 hrs	mackinawite,		Wang and Morse, 1996
n.i.	17.60	**	5.06	~4320 hrs	greigite,	XRD, SEM	
n.i.	66.50		5.01	~4320 hrs	pyrite		
41.60	8.10	5.14	7.00	~168 hrs	mackinawite,	Mössbauer spectroscopy	Wan et al., 2017
3.40	14.90	0.23	7.00	~3672 hrs	pyrite		
112.36	224.72	0.50	7.20	~336 hrs	mackinawite	XANES	Kumar et al., 2018
112.36	112.36	1.00			mackinawite		
11.20	11.20	1.00	6.00	~1056 hrs	mackinawite, greigite, pyrite	XRD, SEM, TEM	This study

562 Note: c_{Fe} and $c_{S(-II)}$ are given in mM. “n.i.” stands for “not indicated”, and ** indicates “S(-II)
563 in excess”.

564 Mackinawite was identified in most studies listed in Table 2, and was consistently
565 described as resulting from aging or crystallization of amorphous FeS_x precursors, that
566 would result from direct coprecipitation of Fe(II) and S(-II) according to Eq. 2 (Rickard,
567 1975; Schoonen and Barnes, 1991a). Both lower (< 7.0) pH conditions (Wang and
568 Morse, 1996) and decreased Fe:S(-II) ratios (Kumar et al., 2018) increase dissolution
569 rate of iron (oxyhydr)oxides and mackinawite precipitation rate. Although mackinawite
570 readily precipitates in all runs of the present study, it hardly accumulates during
571 sulfidation, compared to greigite and pyrite (Fig. 2 and Table S1). Two hypotheses may
572 account for this specific behavior: i) the swift consumption of dissolved S(-II) (Fig. 6a)
573 leads to low S(-II) levels, insufficient to precipitate mackinawite but allowing pyrite
574 formation to proceed (Rickard and Luther, 2007); ii) mackinawite acts as a precursor
575 for the formation of both greigite and pyrite (Wang and Morse, 1996). In addition, the
576 initial formation of mackinawite provides active surfaces that favor pyrite nucleation
577 and growth (Rickard and Luther, 2007), inhibiting further mackinawite formation and

578 growth. Mackinawite was also reported to be a necessary precursor for greigite
579 formation (Rickard and Luther, 2007) through a rearrangement of Fe atoms in a [S(-II)]
580 cubic close packing lattice and Fe loss to reach a proper Fe:S ratio (Lennie et al., 1997).

581 Formation of greigite along goethite sulfidation derived from XRD data analysis
582 in the present work (Fig. 1) was consistently reported only by Wang and Morse (1996)
583 in similar sulfidation experiments. In contrast, the presence of greigite was rejected in
584 other studies from the analysis of Mössbauer spectra (Wan et al., 2017) or from the
585 modeling of S K-edge XANES (X-ray absorption near edge structure) data (Kumar et
586 al., 2018). These contrasting results suggest the key role of initial solution pH for
587 greigite formation; sulfidation experiments of Wang and Morse (1996) were performed
588 indeed under weakly acidic conditions consistent with the present ones (pH = 5.0 and
589 6.0, respectively), whereas those of Wan et al. (2017) and Kumar et al. (2018) were
590 performed under circum-neutral conditions (pH = 7.0 or 7.2). Contrary to the present
591 hypothesis derived from the comparison of experimental studies, Son et al. (2022)
592 predicted from Density Functional Theory calculations that greigite stability and
593 formation would be favored by higher pH conditions. These calculations were
594 performed however for nanometer sized particles (~0.5-4 nm) to benefit from greigite
595 lower surface energy compared to pyrite. In the present study, Rietveld refinement of
596 XRD data indicates much larger crystal sizes (~15-18 nm along the 001 axis) for
597 greigite. The Fe:S ratio appears less influential for greigite precipitation as Kumar et al.
598 (2018) performed their experiments using a Fe:S ratio similar to that of the present
599 study (Fe:S molar ratio ≈ 1).

600 Pyrite was formed in most goethite sulfidation experiments reported in the
601 literature. Slightly alkaline conditions and low Fe:S(-II) ratios appear however to
602 hamper pyrite formation (Kumar et al., 2018; Pyzik and Sommer, 1981; Rickard, 1974;
603 Wan et al., 2017). Duration of the sulfidation experiment also appears as an important
604 parameter for pyrite formation. Pyrite was not detected by Rickard (1974) and Pyzik
605 and Sommer (1981) whose goethite sulfidation experiments lasted ~2 and ~24 hrs,
606 respectively, whereas a minor amount of pyrite (~1-2%) was detected only after ~48
607 hrs by Wan et al. (2017) using Mössbauer spectroscopy, consistent with the present

608 study in which minor pyrite (~1-2 wt.%) was detected in sulfidation products after 3
609 days (Figs. 2, 3, and S1). In the present sulfidation experiments, pyrite formed
610 massively from 3-7 days (Figs. 2, 3, S1, and S2). Low Fe:S(-II) ratios (≤ 0.2) may delay
611 further pyrite formation as shown by the presence of pyrite being detected only after
612 ~56-60 days under such experimental conditions (Wan et al., 2017; Wang and Morse,
613 1996). Despite favorable Fe:S(-II) ratio (0.5-1.0) and sufficient duration (14 days),
614 Kumar et al. (2018) discarded pyrite presence among goethite sulfidation products from
615 the analysis of S K-edge XANES data. Contrasting initial solution pH values (7.2 vs.
616 6.0 in the present experiments) are most likely responsible for the much higher pyrite
617 contents reported in the present experiments (~28.5-39.1% after 7-25 days – Fig. 2 and
618 Table S1), consistent with the results of Wang and Morse (1996). Although pyrite is the
619 dominant iron sulfide in most geological settings, Fe sulfidation or pyritization appears
620 incomplete in many cases, with the persistence of MIS. Apart from the unfavorable
621 conditions described above [low Fe:S(-II) ratio, slightly alkaline pH conditions], low
622 concentration of S^0 in solution (Fig. 6c) may also hamper MIS transformation to pyrite
623 Wang and Morse (1996).

624 Consistently, colloidal FeS (or FeS_x clusters) were readily formed upon addition
625 of goethite into the S(-II)-containing solutions, as the solution got black immediately
626 after the addition (Hellige et al., 2012; Hockmann et al., 2020; Noël et al., 2020; Peiffer
627 et al., 2015; Rickard, 1974), even after filtration through 0.22 μm nylon filters (not
628 shown). Solutions remained black-colored for about one week before turning colorless
629 consistent with previous observations from ferrihydrite sulfidation (Noël et al., 2020).
630 The timing of this color change roughly coincides with the remarkable decrease of S^0
631 (Fig. 6c) and with the onset of the three crystalline iron sulfides identified by XRD in
632 the present experiments (Fig. 2 and Table S1). This coincidence suggests that reaction
633 between colloidal FeS (or FeS_x clusters) and S^0 according to Eq. 2 most likely
634 contributed to or even dominated the early formation of pyrite from goethite sulfidation
635 (Hellige et al., 2012; Peiffer et al., 2015).

636 4.2 Influence of Ni on the sulfidation of goethite to pyrite

637 In this study, the influence of both adsorbed and structurally incorporated Ni on/in
638 goethite on its sulfidation was assessed. The limited modification of Fe local
639 environment in sulfidized Ni-bearing samples compared to Ni-free one (Figs. 3, S2, and
640 S3) and the slower formation of pyrite (Fig. S1, Table S1) suggest that the presence of
641 Ni hampered goethite sulfidation. Consistently, after 44 days of interaction with S(-II),
642 reaction products of Ni-free goethite contain significantly more pyrite (54.4% vs.
643 33.2%, 33.5%, 33.0%, and 40.7%, Table S1) and less MIS (4.2% vs. 12.7%, 12.7%,
644 16.5%, and 11.7%, Table S1) than their counterparts from Ni-bearing goethites. A
645 similar trend may be observed after 25 days of reaction (Fig. 2 and Table S1), suggesting
646 that Ni stabilized MIS and delayed their complete conversion to pyrite, consistent with
647 previous report (Swanner et al., 2019).

648 After the swift pyrite formation from 3-7 days in both Ni-free and -containing
649 experiments, pyrite formation proceeded gradually (Fig. 2 and Table S1), indicating that
650 MIS likely mediated this process at this later stage (Luther, 1991; Rickard and Luther,
651 2007), as colloidal FeS and FeS_x clusters almost disappeared. During the pyritization
652 process, destabilization of both FeS_x clusters / colloidal FeS and MIS release Fe(II),
653 likely contributing to the increase of [Fe(II)] in solution within the first ~15 days of
654 reaction [Fig. 6b - (Butler and Rickard, 2000; Lennie et al., 1997)]. For all runs, the
655 content of MIS was kept at a relatively low level (<2.7%) before 7 days, while after that
656 MIS in Ni-containing groups accumulated up to 11.7%-16.6%. In contrast, MIS content
657 in the Ni-free experiment only reached 4.2%, suggesting again that their association
658 with Ni hindered the conversion of MIS to pyrite after 7 days.

659 The negative impact of Ni on MIS transformation to pyrite started earlier however.
660 After 3 days of interaction with S(-II), iron sulfide formation is extremely marginal in
661 all cases but modification of Fe local environment appears to be more limited in Ni-
662 bearing goethites compared to Gt (Fig. S3). This reduced modification suggests also
663 that the presence of Ni, both as adsorbed and incorporated species, decreases goethite
664 reactivity towards S(-II). As proposed previously (Xu et al., 2006), the presence of Ni(II)

665 sorbed at the goethite surface possibly hinders subsequent sorption of other ions [S(-II)
666 in this study]. In addition, the reduced surface charge resulting from Ni(II)-for-Fe(III)
667 substitutions could also contribute to decrease goethite reactivity (de Carvalho-E-Silva
668 et al., 2002). It should be noted however that in the present study similar kinetics of S(-
669 II) consumption was measured for all reacting samples up to 3 days (Fig. 6a). This
670 apparent inconsistency likely results from the fast decrease of S(-II) content originating
671 from S(-II) adsorption to goethite surface, precipitation with Fe(II) and Ni(II), and
672 formation of colloidal FeS and FeS_x clusters, making adsorption specific contribution
673 difficult to differentiate.

674 Mackinawite and FeS_x cluster formation is considered to result from the direct
675 coprecipitation of Fe(II) with S(-II) (Rickard and Luther, 2007), and dissolved Ni(II)
676 precipitates more readily with S(-II) compared to Fe(II) [5.89×10^{-10} vs. 2.29×10^{-4} for
677 Ni and Fe, respectively – (Morse and Arakaki, 1993)]. The tendency of Ni to precipitate
678 first as Ni-rich nuclei has been confirmed recently from TEM observations (Mansor et
679 al., 2019), consistent with the present distribution of Ni in MIS particles (Figs. 7 and
680 S5). In addition, mackinawite crystal growth rate increases in the presence of Ni(II),
681 crystal structure being stabilized by Ni(II) (Ikogou et al., 2017). In the present work,
682 mackinawite content remains limited in all experiments although the maximum
683 mackinawite content [8.0(2) wt.%] was reported for GtANi20-44d (Table S1). The
684 presence of Ni(II) appears to stabilize MIS as a whole (Fig. 2 and Table S1) however,
685 possibly inhibiting their conversion to pyrite. The limited mackinawite content also
686 suggests that the mackinawite-to-greigite transformation was not significantly hindered
687 by Ni thus hampering the identification of a possible positive effect on mackinawite
688 formation.

689 **4.3 The migration of Ni from goethite to iron sulfides**

690 The systematic correlation between Ni and Fe sulfide polycrystals observed with
691 electron microscopy (Figs. 7 and S5) evidenced the migration of Ni initially associated
692 to goethite to iron sulfides (pyrite mainly) resulting from the sulfidation thereof. Acid
693 treatments using HCl suggest however that Ni distribution within MIS depends on the

694 initial association mode of Ni with goethite. When initially incorporated in goethite
695 structure, Ni is homogeneously distributed in newly formed sulfides whereas Ni
696 appears to be enriched in MIS crystal cores when initially adsorbed onto goethite (Fig.
697 8c), consistent with previous reports (Mansor et al., 2019). In contrast, subsequent acid
698 treatments using HNO₃ indicate that Ni was homogeneously distributed in newly
699 formed pyrite, regardless of the initial association mode of Ni with goethite (Fig. 9c).
700 It should be noted that Ni was not detected in solution during sulfidation of Ni-bearing
701 goethite, implying that this process does not contribute Ni to sedimentary pore water in
702 geological settings. In addition, the absence of dissolved Ni suggests that contrasting
703 Ni distributions observed as a function of the initial association mode of Ni with
704 goethite derive from differences in Ni and Fe release rates during the sulfidation of
705 goethites. Specifically, adsorbed Ni(II) is most likely released faster compared to
706 structural Fe, the latter being gradually released during goethite reductive dissolution.
707 In addition, Ni(II) precipitates with S(-II) faster than Fe(II) (Morse and Arakaki, 1993)
708 and thus concentrates mainly in the inner part of mackinawite particles. In contrast,
709 Ni(II) structurally incorporated in GtNi₆ was released almost stoichiometrically with
710 Fe(II), resulting in a homogeneous distribution of both metals within MIS crystals.

711 Although Ni(II) may be heterogeneously distributed within MIS crystals, its
712 distribution within pyrite systematically appears to be homogeneous as suggested by
713 the congruent release of Ni and Fe along the late (> 24 hrs) HCl and the whole HNO₃
714 acid treatments (Fig. 9c). This homogenous distribution in pyrite appears logical when
715 MIS precursors also exhibit a homogeneous Ni distribution, owing to Fe(II) and Ni(II)
716 interaction with S₂(-II) onto mackinawite and greigite active surfaces to form pyrite
717 (Rickard and Luther, 2007). In MIS formed from Ni-adsorbed goethite, Ni distribution
718 is heterogeneous however, and redistribution of Ni between mackinawite and greigite
719 most likely accounts for this apparent inconsistency. Specifically, mackinawite-to-
720 greigite conversion is likely responsible for this redistribution before the subsequent
721 formation of pyrite, as this conversion was described as the rearrangement of Fe (and
722 Ni in the present study) atoms in a cubic close packing S(-II) lattice (Rickard and Luther,
723 2007). As a consequence and although a direct mackinawite-to-pyrite conversion was

724 proposed (Rickard, 1975), the formation of a greigite intermediate appears to be an
725 efficient alternative pathway for pyrite formation from mackinawite, greigite
726 occurrence increasing significantly pyrite formation rate (Lennie et al., 1997; Wang and
727 Morse, 1996).

728 **4.4 Geochemical and environmental implications**

729 In natural soil environments, Ni concentration usually increases with increasing
730 depth (Michopoulos, 2021), goethite [and other iron (oxyhydr)oxides] and iron sulfides
731 being common Fe-bearing minerals in upper and deeper horizons, respectively, both
732 being Ni sinks (Ikogou et al., 2017; Morin et al., 2017; Swanner et al., 2019). Goethite
733 is the main Ni host in oxide-type laterite deposits, which accounts for ~70% of Ni
734 world's resources (Landers et al., 2009), the remaining ~30% being hosted in sulfide
735 deposits. Although structural Ni incorporation usually prevails over surface
736 complexation in both cases, Ni release to solution and/or transport to other phases can
737 occur as the result of mineral dissolution or alteration under oxidative (Larsen and
738 Postma, 1997; Nesbitt and Muir, 1994) or reductive (Landers and Gilkes, 2007; Landers
739 et al., 2009) conditions. From the present results, Ni association to goethite slows down
740 its possible conversion to Fe sulfides under reducing conditions, possibly accounting
741 for goethite persistence in thermodynamically unfavorable S(-II)-rich conditions. Ni
742 migration from Fe (oxyhydr)oxides to Fe sulfides along goethite sulfidation as reported
743 in the present work most likely represents the main transport pathway for Ni from the
744 oxic zone to the anoxic zone however. In turn, the swift release of Ni to solution upon
745 the oxidative alteration of Ni-bearing Fe sulfides, in acid mine drainage for example, is
746 a key process of Ni geochemical cycling.

747 **Conclusions**

748 The mineralogical evolution observed in the present study along goethite
749 sulfidation is consistent with the commonly accepted reaction mechanisms for this
750 process. The mineralogical sequence, and thus mechanisms at play, is similar for both
751 Ni-free and Ni-containing goethites and involves the swift initial formation of colloidal

752 FeS, FeS_x clusters, and metastable iron sulfides (mackinawite and greigite) prior to
753 pyrite formation that is detected after ~3 days of interaction with S(-II). The early (~3-
754 7 days) formation of pyrite originates from the reaction between colloidal FeS, FeS_x
755 clusters, and S⁰, and the later stage (~7-44 days) mainly comes from the conversion of
756 metastable iron sulfides. Consistent with previous reports, greigite formation appears
757 to be favored by slightly acidic pH conditions (pH = 6.0). These conditions also enhance
758 pyrite crystallization, whereas low Fe:S(-II) ratios (≤ 0.2) negatively impact pyrite
759 formation. Compared to the Ni-free system, pyrite formation rate is also decreased by
760 the presence of Ni, independent of its association mode with goethite, i.e., adsorption
761 or isomorphic substitution. Ni appears indeed to reduce the reactivity of goethite to S(-
762 II) and increase MIS stability, the overall sulfidation progress, as measured by Fe local
763 environment and the relative proportion of sulfides and goethite, being similar in all
764 cases. Incorporation of Ni in intermediate MIS also buffers its subsequent release and
765 induces a uniform distribution of this element in newly formed pyrite, independent of
766 its initial association mode with goethite.

767 **Acknowledgements**

768 This work is supported by the National Natural Science Foundations of China (No.
769 42107319, 42225704, and 42077290). We are grateful to Dr. Zhongjun Chen and Dr.
770 Yunpeng Liu at BSRF for their assistance with Fe K-edge XAFS data collection and
771 analysis, and we thank Dr. Jiang Xu at Zhejiang University for providing XAFS
772 standards of pyrite and mackinawite, and Dr. Shuang Zhang at Huazhong Agricultural
773 University is appreciated for her help with XRD data collection. Dr. Vincent Noël
774 kindly provided the EXAFS reference spectrum of colloidal FeS. ISTERre is part of
775 Labex OSUG@2020 (ANR10-LABX56).

776 **Research Data**

777 Research Data related to this article includes: Chemical compositions; XRD data;
778 XAS data at Fe K-edges; TGA data; Solution chemistry; Fe/Ni release upon HCl/HNO₃
779 treatment. Dataset can be accessed at Mendeley Data, V1, doi: 10.17632/khhhyhkhjz.1.

780 **Appendix A. Supplementary Material**

781 Supplementary material includes i) XRD patterns showing the mineralogical
782 evolution of goethite samples as a function of sulfidation duration and results of
783 Rietveld refinements performed on this data (quantitative phase analysis and unit-cell
784 parameters of the main minerals present), ii) Fe K-edge EXAFS spectra of pritsine and
785 sulfidized goethite samples and difference thereof, iii) TEM micrographs, SAED, and
786 STEM-HAADF data obtained on sulfidized samples, and iv) modeling of Fe and Ni
787 kinetic release upon HCl treatment of goethite samples.

788

789 **References**

790

- 791 Bagarinao T. (1992) Sulfide as an environmental factor and toxicant: tolerance and
792 adaptations in aquatic organisms. *Aquat. Toxicol.* **24**, 21-62.
- 793 Biber M. V., dos Santos Afonso M. and Stumm W. (1994) The coordination chemistry
794 of weathering: IV. Inhibition of the dissolution of oxide minerals. *Geochim.*
795 *Cosmochim. Acta* **58**, 1999-2010.
- 796 Bishop D. W., Thomas P. S. and Ray A. S. (1999) α - β Phase Re-Transformation Kinetics
797 in Nickel Sulphide. *J. Therm. Anal. Calorim.* **56**, 429-435.
- 798 Burton E. D., Johnston S. G., Watling K., Bush R. T., Keene A. F. and Sullivan L. A.
799 (2010) Arsenic Effects and Behavior in Association with the Fe(II)-Catalyzed
800 Transformation of Schwertmannite. *Environ. Sci. Technol.* **44**, 2016-2021.
- 801 Butler I. B. and Rickard D. (2000) Framboidal pyrite formation via the oxidation of
802 iron (II) monosulfide by hydrogen sulphide. *Geochim. Cosmochim. Acta* **64**,
803 2665-2672.
- 804 Canfield D. E. (1989) Reactive iron in marine sediments. *Geochim. Cosmochim. Acta*
805 **53**, 619-632.
- 806 Canfield D. E., Raiswell R. and Bottrell S. H. (1992) The reactivity of sedimentary iron
807 minerals toward sulfide. *Am. J. Sci.* **292**, 659-683.
- 808 Cao F., Hu W., Zhou L., Shi W., Song S., Lei Y., Wang S. and Zhang H. (2009) 3D
809 Fe₃S₄ flower-like microspheres: high-yield synthesis via a biomolecule-
810 assisted solution approach, their electrical, magnetic and electrochemical
811 hydrogen storage properties. *Dalton Trans.* 10.1039/b912569h, 9246-9252.
- 812 Cline J. D. (1969) Spectrophotometric determination of hydrogen sulfide in natural
813 waters I. *Limnol. Oceanogr.* **14**, 454-458.
- 814 Cooper D. C. and Morse J. W. (1998) Extractability of Metal Sulfide Minerals in Acidic
815 Solutions: Application to Environmental Studies of Trace Metal Contamination

816 within Anoxic Sediments. *Environ. Sci. Technol.* **32**, 1076-1078.

817 Cornell R. M. (1991) Simultaneous incorporation of Mn, Ni and Co in the goethite
818 (alpha-FeOOH) structure. *Clay Miner.* **26**, 427-430.

819 Cornell R. M. and Schwertmann U. (2004) *The Iron Oxides: Structure, Properties,*
820 *Reactions, Occurrences and Uses, Second Edition.*

821 Cornwell J. C. and Morse J. W. (1987) The characterization of iron sulfide minerals in
822 anoxic marine sediments. *Mar. Chem.* **22**, 193-206.

823 de Carvalho-E-Silva M. L. M., Partiti C. S. M., Enzweiler J., Petit S., Netto S. M. and
824 de Oliveira S. M. B. (2002) Characterization of Ni-containing goethites by
825 Mossbauer spectroscopy and other techniques. *Hyperfine Interact.* **142**, 559-576.

826 Deoliveira S. M. B., Trescases J. J. and Melfi A. J. (1992) Lateritic Nickel deposits of
827 Brazil. *Miner. Deposita* **27**, 137-146.

828 Döbelin N. (2015) Interlaboratory study on the quantification of calcium phosphate
829 phases by Rietveld refinement. *Powder Diffr.* **30**, 231-241.

830 Döbelin N. and Kleeberg R. (2015) Profex: a graphical user interface for the Rietveld
831 refinement program BGMN. *J. Appl. Crystallogr.* **48**, 1573-1580.

832 Dos Santos Afonso M. and Stumm W. (1992) Reductive dissolution of iron(III)
833 (hydr)oxides by hydrogen sulfide. *Langmuir* **8**, 1671-1675.

834 Du R., Xian H., Wu X., Zhu J., Wei J., Xing J., Tan W. and He H. (2021) Morphology
835 dominated rapid oxidation of framboidal pyrite. *Geochem. Perspect. Let.* **16**,
836 53-58.

837 Dubbin W. E. and Bullough F. (2017) Dissolution of Al-Substituted Goethite in the
838 Presence of Ferrichrome and Enterobactin at pH 6.5. *Aquat. Geochem.* **23**, 61-
839 74.

840 Dublet G., Juillot F., Morin G., Fritsch E., Fandeur D. and Brown Jr G. E. (2015)
841 Goethite aging explains Ni depletion in upper units of ultramafic lateritic ores
842 from New Caledonia. *Geochim. Cosmochim. Acta* **160**, 1-15 %@ 0016-7037.

843 Dublet G., Juillot F., Morin G., Fritsch E., Fandeur D., Ona-Nguema G. and Brown Jr
844 G. E. (2012) Ni speciation in a New Caledonian lateritic regolith: a quantitative
845 X-ray absorption spectroscopy investigation. *Geochim. Cosmochim. Acta* **95**,
846 119-133.

847 Dunn J. G. and Kelly C. E. (1977) A TG/DTA/MS study of the oxidation of nickel
848 sulphide. *J. Therm. Anal.* **12**, 43-52.

849 Elias M. (2002) Nickel laterite deposits – geological overview, resources and
850 exploitation.

851 Eliopoulos D. G. and Economou-Eliopoulos M. (2000) Geochemical and mineralogical
852 characteristics of Fe–Ni- and bauxitic-laterite deposits of Greece. *Ore Geol. Rev.*
853 **16**, 41-58.

854 Fadrus H. and Malý J. (1975) Suppression of iron(III) interference in the determination
855 of iron(II) in water by the 1,10-phenanthroline method. *Analyst* **100**, 549-554.

856 Fan R. and Gerson A. R. (2015) Synchrotron micro-spectroscopic examination of
857 Indonesian nickel laterites. *Am. Mineral.* **100**, 926-934.

858 Frierdich A. J., McBride A., Tomkinson S. and Southall S. C. (2019) Nickel Cycling
859 and Negative Feedback on Fe(II)-Catalyzed Recrystallization of Goethite. *ACS*

860 *Earth Space Chem.* **3**, 1932-1941.

861 Gasser U. G., Jeanroy E., Mustin C., Barres O., Nuesch R., Berthelin J. and Herbillon
862 A. J. (1996) Properties of synthetic goethites with Co for Fe substitution. *Clay*
863 *Miner.* **31**, 465-476.

864 Girgin I., Obut A. and Ucyildiz A. (2011) Dissolution behaviour of a Turkish lateritic
865 nickel ore. *Miner. Eng.* **24**, 603-609.

866 Hellige K., Pollok K., Larese-Casanova P., Behrends T. and Peiffer S. (2012) Pathways
867 of ferrous iron mineral formation upon sulfidation of lepidocrocite surfaces.
868 *Geochim. Cosmochim. Acta* **81**, 69-81.

869 Hockmann K., Planer-Friedrich B., Johnston S. G., Peiffer S. and Burton E. D. (2020)
870 Antimony mobility in sulfidic systems: Coupling with sulfide-induced iron
871 oxide transformations. *Geochim. Cosmochim. Acta* **282**, 276-296.

872 Hohmann C., Morin G., Ona-Nguema G., Guigner J. M., Brown G. E. and Kappler A.
873 (2011) Molecular-level modes of As binding to Fe(III) (oxyhydr)oxides
874 precipitated by the anaerobic nitrate-reducing Fe(II)-oxidizing *Acidovorax* sp
875 strain BoFeN1. *Geochim. Cosmochim. Acta* **75**, 4699-4712.

876 Huang F.-G., Jia S.-Y., Liu Y., Wu S.-H. and Han X. (2015) Reductive dissolution of
877 ferrihydrite with the release of As(V) in the presence of dissolved S(-II). *J.*
878 *Hazard. Mater.* **286**, 291-297.

879 Huerta-Diaz M. A. and Morse J. W. (1990) A quantitative method for determination of
880 trace metal concentrations in sedimentary pyrite. *Mar. Chem.* **29**, 119-144.

881 Hurtgen M. T., Lyons T. W., Ingall E. D. and Cruse A. M. (1999) Anomalous
882 enrichments of iron monosulfide in euxinic marine sediments and the role of
883 H₂S in iron sulfide transformations: Examples from Effingham Inlet, Orca
884 Basin, and the Black Sea. *Am. J. Sci.* **299**, 556-588.

885 Ikogou M., Ona-Nguema G., Juillot F., Le Pape P., Menguy N., Richeux N., Guigner J.
886 M., Noel V., Brest J., Baptiste B. and Morin G. (2017) Long-term sequestration
887 of nickel in mackinawite formed by *Desulfovibrio capillatus* upon Fe(III)-citrate
888 reduction in the presence of thiosulfate. *Appl. Geochem.* **80**, 143-154.

889 Islam M. and Patel R. (2017) Solvothermal synthesis of greigite (Fe₃S₄)- Conducting
890 polypyrrole nanocomposite and its application towards arsenic removal. *Sep.*
891 *Sci. Technol.* **52**, 2835-2852.

892 Kalatha S. and Economou-Eliopoulos M. (2015) Framboidal pyrite and bacterio-
893 morphic goethite at transitional zones between Fe-Ni-laterites and limestones:
894 Evidence from Lokris, Greece. *Ore Geol. Rev.* **65**, 413-425.

895 Kraal P., Burton E. D. and Bush R. T. (2013) Iron monosulfide accumulation and pyrite
896 formation in eutrophic estuarine sediments. *Geochim. Cosmochim. Acta* **122**,
897 75-88.

898 Krs M., Novak F., Krsova M., Pruner P. and Jansa J. (1993) Magnetic-properties, self-
899 reversal remanence and thermal alteration products of smythite *Stud. Geophys.*
900 *Geod.* **37**, 382-400.

901 Kumar N., Pacheco J. L., Noel V., Dublet G. and Brown G. E. (2018) Sulfidation
902 mechanisms of Fe(III)-(oxyhydr)oxide nanoparticles: a spectroscopic study.
903 *Environ. Sci. Nano* **5**, 1012-1026.

- 904 Kyprianidou-Leodidou T., Althaus H. J., Wyser Y., Vetter D., Buchler M., Caseri W. and
905 Suter U. W. (1997) High refractive index materials of iron sulfides and
906 poly(ethylene oxide). *J. Mater. Res.* **12**, 2198-2206.
- 907 Lan Y. and Butler E. C. (2014) Monitoring the transformation of mackinawite to greigite
908 and pyrite on polymer supports. *Appl. Geochem.* **50**, 1-6.
- 909 Landers M. and Gilkes R. J. (2007) Dehydroxylation and dissolution of nickeliferous
910 goethite in New Caledonian lateritic Ni ore. *Appl. Clay Sci.* **35**, 162-172.
- 911 Landers M., Gilkes R. J. and Wells M. (2009) Dissolution kinetics of dehydroxylated
912 nickeliferous goethite from limonitic lateritic nickel ore. *Appl. Clay Sci.* **42**,
913 615-624.
- 914 Larsen F. and Postma D. (1997) Nickel mobilization in a groundwater well field: release
915 by pyrite oxidation and desorption from manganese oxides. *Environ. Sci.*
916 *Technol.* **31**, 2589-2595.
- 917 Larsen O. and Postma D. (2001) Kinetics of reductive bulk dissolution of lepidocrocite,
918 ferrihydrite, and goethite. *Geochim. Cosmochim. Acta* **65**, 1367-1379.
- 919 Lennie A. R., Redfern S. A. T., Champness P. E., Stoddart C. P., Schofield P. F. and
920 Vaughan D. J. (1997) Transformation of mackinawite to greigite: An in situ X-
921 ray powder diffraction and transmission electron microscope study. *Am.*
922 *Mineral.* **82**, 302-309.
- 923 Liu J., Pellerin A., Wang J., Rickard D., Antler G., Zhao J., Wang Z., Jørgensen B. B.
924 and Ono S. (2022) Multiple sulfur isotopes discriminate organoclastic and
925 methane-based sulfate reduction by sub-seafloor pyrite formation. *Geochim.*
926 *Cosmochim. Acta* **316**, 309-330.
- 927 Lowers H. A., Breit G. N., Foster A. L., Whitney J., Yount J., Uddin N. and Muneem A.
928 (2007) Arsenic incorporation into authigenic pyrite, bengal basin sediment,
929 Bangladesh. *Geochim. Cosmochim. Acta* **71**, 2699-2717.
- 930 Luther G. W. (1991) Pyrite synthesis via polysulfide compounds. *Geochim. Cosmochim.*
931 *Acta* **55**, 2839-2849.
- 932 Manceau A., Schlegel M. L., Musso M., Sole V. A., Gauthier C., Petit P. E. and Trolard
933 F. (2000) Crystal chemistry of trace elements in natural and synthetic goethite.
934 *Geochim. Cosmochim. Acta* **64**, 3643-3661.
- 935 Mansor M., Winkler C., Hochella M. F., Jr. and Xu J. (2019) Nanoparticulate Nickel-
936 Hosting Phases in Sulfidic Environments: Effects of Ferrous Iron and Bacterial
937 Presence on Mineral Formation Mechanism and Solid-Phase Nickel
938 Distribution. *Front. Earth Sci.* **7**.
- 939 Maurice P. A., Lee Y. J. and Hersman L. E. (2000) Dissolution of Al-substituted
940 goethites by an aerobic *Pseudomonas mendocina* var. bacteria. *Geochim.*
941 *Cosmochim. Acta* **64**, 1363-1374.
- 942 Michopoulos P. (2021) Nickel in forests - a short review on its distribution and fluxes.
943 *Folia Oecologica* **48**, 205-214.
- 944 Morin G., Noel V., Menguy N., Brest J., Baptiste B., Tharaud M., Ona-Nguema G.,
945 Ikogou M., Viollier E. and Juillot F. (2017) Nickel accelerates pyrite nucleation
946 at ambient temperature. *Geochem. Perspect. Lett.* **5**, 6-11.
- 947 Morse J. W. and Arakaki T. (1993) Adsorption and coprecipitation of divalent metals

948 with mackinawite (FeS). *Geochim. Cosmochim. Acta* **57**, 3635-3640.

949 Morse J. W. and Luther G. W. (1999) Chemical influences on trace metal-sulfide
950 interactions in anoxic sediments. *Geochim. Cosmochim. Acta* **63**, 3373-3378.

951 Morse J. W., Millero F. J., Cornwell J. C. and Rickard D. (1987) The chemistry of the
952 hydrogen sulfide and iron sulfide systems in natural waters. *Earth Sci. Rev.* **24**,
953 1-42.

954 Nachtegaal M. and Spark D. L. (2002) Kinetics and mechanisms of nickel surface
955 precipitation in multi-sorbent system: a spectroscopic study. *In: 17th WCSS,*
956 *Thailand*, 1345-1355.

957 Nesbitt H. W. and Muir I. J. (1994) X-ray photoelectron spectroscopic study of a pristine
958 pyrite surface reacted with water-vapor and air. *Geochim. Cosmochim. Acta* **58**,
959 4667-4679.

960 Noël V., Kumar N., Boye K., Barragan L., Lezama-Pacheco J. S., Chu R., Tolic N.,
961 Brown G. E. and Bargar J. R. (2020) FeS colloids - formation and mobilization
962 pathways in natural waters. *Environ. Sci. Nano* **7**, 2102-2116.

963 Noël V., Morin G., Juillot F., Marchand C., Brest J., Bargar J. R., Munoz M., Marakovic
964 G., Ardo S. and Brown G. E., Jr. (2015) Ni cycling in mangrove sediments from
965 New Caledonia. *Geochim. Cosmochim. Acta* **169**, 82-98.

966 Otero X. L., Ferreira T. O., Huerta-Diaz M. A., Partiti C. S. M., Souza V., Vidal-Torrado
967 P. and Macias F. (2009) Geochemistry of iron and manganese in soils and
968 sediments of a mangrove system, Island of Pai Matos (Cananeia - SP, Brazil).
969 *Geoderma* **148**, 318-335.

970 Peiffer S., Behrends T., Hellige K., Larese-Casanova P., Wan M. and Pollok K. (2015)
971 Pyrite formation and mineral transformation pathways upon sulfidation of ferric
972 hydroxides depend on mineral type and sulfide concentration. *Chem. Geol.* **400**,
973 44-55.

974 Ponomar V. P. (2018) Thermomagnetic properties of the goethite transformation during
975 high-temperature treatment. *Miner. Eng.* **127**, 143-152.

976 Poulton S. W. (2003) Sulfide oxidation and iron dissolution kinetics during the reaction
977 of dissolved sulfide with ferrihydrite. *Chem. Geol.* **202**, 79-94.

978 Poulton S. W., Krom M. D. and Raiswell R. (2004) A revised scheme for the reactivity
979 of iron (oxyhydr)oxide minerals towards dissolved sulfide. *Geochim.*
980 *Cosmochim. Acta* **68**, 3703-3715.

981 Pyzik A. J. and Sommer S. E. (1981) Sedimentary iron monosulfides: Kinetics and
982 mechanism of formation. *Geochim. Cosmochim. Acta* **45**, 687-698.

983 Ravel B. and Newville M. (2005) ATHENA and ARTEMIS: interactive graphical data
984 analysis using IFEFFIT. *Phys. Scr.* **2005**, 1007.

985 Ren H.-T., Ji Z.-Y., Wu S.-H., Han X., Liu Z.-M. and Jia S.-Y. (2018) Photoreductive
986 dissolution of schwertmannite induced by oxalate and the mobilization of
987 adsorbed As(V). *Chemosphere* **208**, 294-302.

988 Rickard D. (1975) Kinetics and mechanism of pyrite formation at low temperatures.
989 *Am. J. Sci.* **275**, 636-652.

990 Rickard D. and Luther G. W. (2007) Chemistry of Iron Sulfides. *Chem. Rev.* **107**, 514-
991 562.

- 992 Rickard D. T. (1974) Kinetics and mechanism of the sulfidation of goethite. *Am. J. Sci.*
993 **274**, 941-952.
- 994 Sagnotti L. and Winkler A. (1999) Rock magnetism and palaeomagnetism of greigite-
995 bearing mudstones in the Italian peninsula. *Earth Planet. Sci. Lett.* **165**, 67-80.
- 996 Schoonen M. A. A. and Barnes H. L. (1991a) Reactions forming pyrite and marcasite
997 from solution: II. Via FeS precursors below 100 °C. *Geochim. Cosmochim. Acta*
998 **55**, 1505-1514.
- 999 Schoonen M. A. A. and Barnes H. L. (1991b) Reactions forming pyrite and marcasite
1000 from solution: I. Nucleation of FeS₂ below 100°C. *Geochim. Cosmochim. Acta*
1001 **55**, 1495-1504.
- 1002 Seyfferth A. L., Bothfeld F., Vargas R., Stuckey J. W., Wang J., Kearns K., Michael H.
1003 A., Guimond J., Yu X. and Sparks D. L. (2020) Spatial and temporal
1004 heterogeneity of geochemical controls on carbon cycling in a tidal salt marsh.
1005 *Geochim. Cosmochim. Acta* **282**, 1-18.
- 1006 Son S., Hyun S. P., Charlet L. and Kwon K. D. (2022) Thermodynamic stability reversal
1007 of iron sulfides at the nanoscale: Insights into the iron sulfide formation in low-
1008 temperature aqueous solution. *Geochim. Cosmochim. Acta* **338**, 220-228.
- 1009 Suter D., Banwart S. and Stumm W. (1991) Dissolution of hydrous Iron(III) oxides by
1010 reductive mechanisms. *Langmuir* **7**, 809-813.
- 1011 Swanner E. D., Webb S. M. and Kappler A. (2019) Fate of cobalt and nickel in
1012 mackinawite during diagenetic pyrite formation. *Am. Mineral.* **104**, 917-928.
- 1013 Ugwu I. M. and Sherman D. M. (2019) The solubility of goethite with structurally
1014 incorporated nickel and cobalt: Implication for laterites. *Chem. Geol.* **518**, 1-8.
- 1015 Ugwu I. M., Sherman D. M. and Bacon C. G. D. (2019) Sorption of nickel onto goethite
1016 (alpha-FeOOH) and desorption kinetics of aged synthetic Ni-goethite:
1017 Implication for Ni laterite ore. *Chem. Geol.* **509**, 223-233.
- 1018 Wan M., Schroeder C. and Peiffer S. (2017) Fe(III): S(-II) concentration ratio controls
1019 the pathway and the kinetics of pyrite formation during sulfidation of ferric
1020 hydroxides. *Geochim. Cosmochim. Acta* **217**, 334-348.
- 1021 Wang Q. W. and Morse J. W. (1996) Pyrite formation under conditions approximating
1022 those in anoxic sediments .1. Pathway and morphology. *Mar. Chem.* **52**, 99-121.
- 1023 Wells M. A., Fitzpatrick R. W. and Gilkes R. J. (2006) Thermal and mineral properties
1024 of Al-, Cr-, Mn-, Ni- and Ti-substituted goethite. *Clays Clay Miner.* **54**, 176-194.
- 1025 Xu Y., Axe L., Yee N. and Dyer J. A. (2006) Bidentate complexation modeling of heavy
1026 metal adsorption and competition on goethite. *Environ. Sci. Technol.* **40**, 2213-
1027 2218.
- 1028 Yang F., Lai Y. and Song Y. (2019) Determination of the influence of pyrite on coal
1029 spontaneous combustion by thermodynamics analysis. *Process Saf. Environ.*
1030 *Prot.* **129**, 163-167.
- 1031 Zachara J. M., Fredrickson J. K., Smith S. C. and Gassman P. L. (2001) Solubilization
1032 of Fe(III) oxide-bound trace metals by a dissimilatory Fe(III) reducing
1033 bacterium. *Geochim. Cosmochim. Acta* **65**, 75-93.

1034

Supplementary Material to:

Sulfidation of Ni-bearing goethites to pyrite: the effects of Ni and implications for its migration between iron phases

Zhongkuan Wu^a, Tingting Zhang^a, Bruno Lanson^b, Hui Yin^c, Dong
Cheng^a, Peng Liu^d, Feng He^{a,e,*}

^a*College of Environment, Zhejiang University of Technology, Hangzhou 310014,
China*

^b*Univ. Grenoble Alpes, Univ. Savoie Mont Blanc, CNRS, IRD, Univ. Gustave Eiffel,
ISTerre, F-38000 Grenoble, France*

^c*Key Laboratory of Arable Land Conservation (Middle and Lower Reaches of Yangtse
River), Ministry of Agriculture and Rural Affairs, College of Resources and
Environment, Huazhong Agricultural University, Wuhan 430070, China*

^d*School of Environmental Studies & State Key Laboratory of Biogeology and
Environmental Geology, China University of Geosciences, Wuhan 430074, China*

^e*Environment and Civil Engineering, Jiangnan University, Wuxi, Jiangsu, 214122,
China*

Corresponding author.

E-mail address: fenghe@zjut.edu.cn (Feng He).

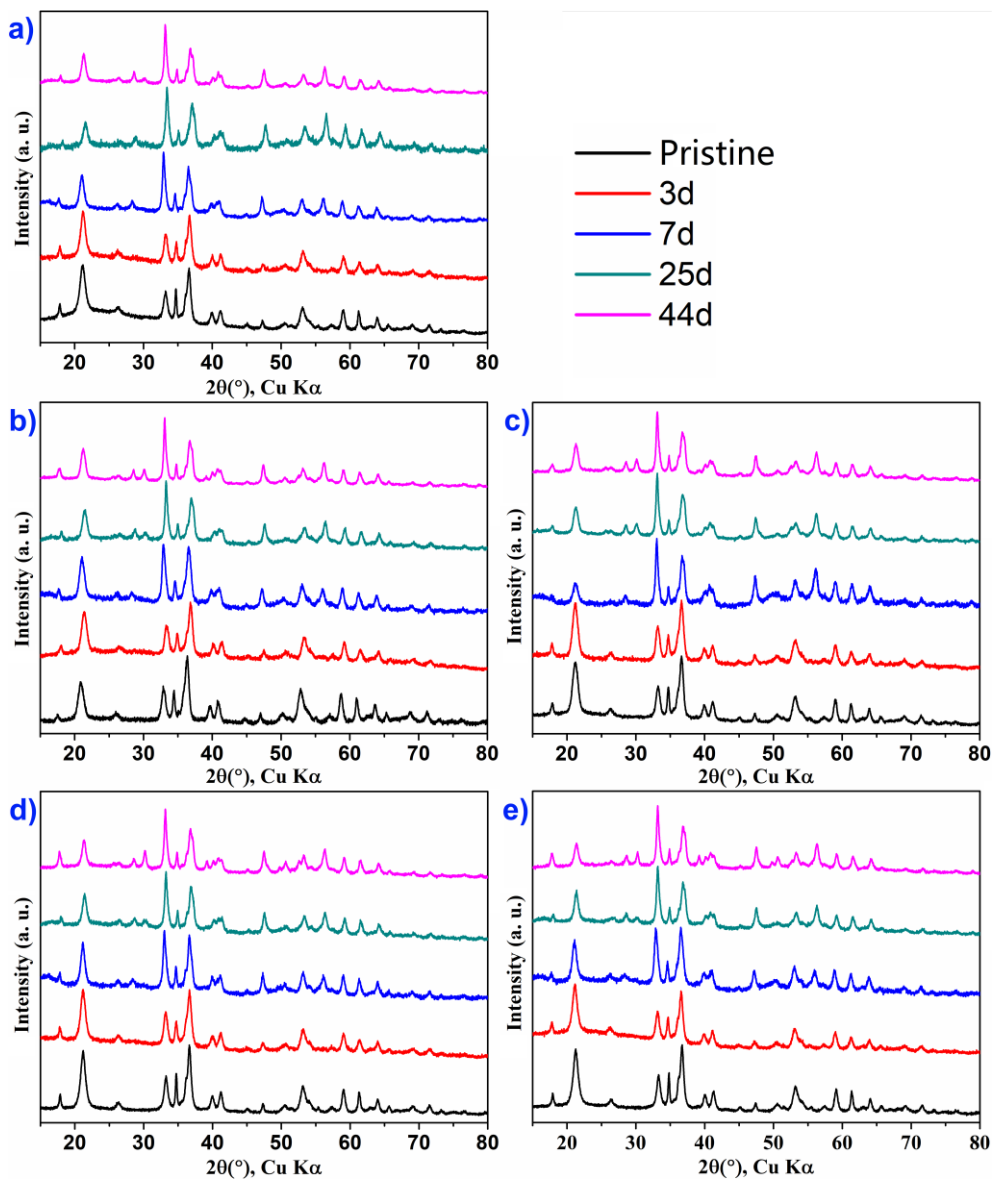


Fig. S1. Evolution of XRD patterns of Ni-free/-containing goethites as a function of sulfidation duration: a) Gt, b) GtNi2, c) GtNi6, d) GtANi5, and e) GtANi20.

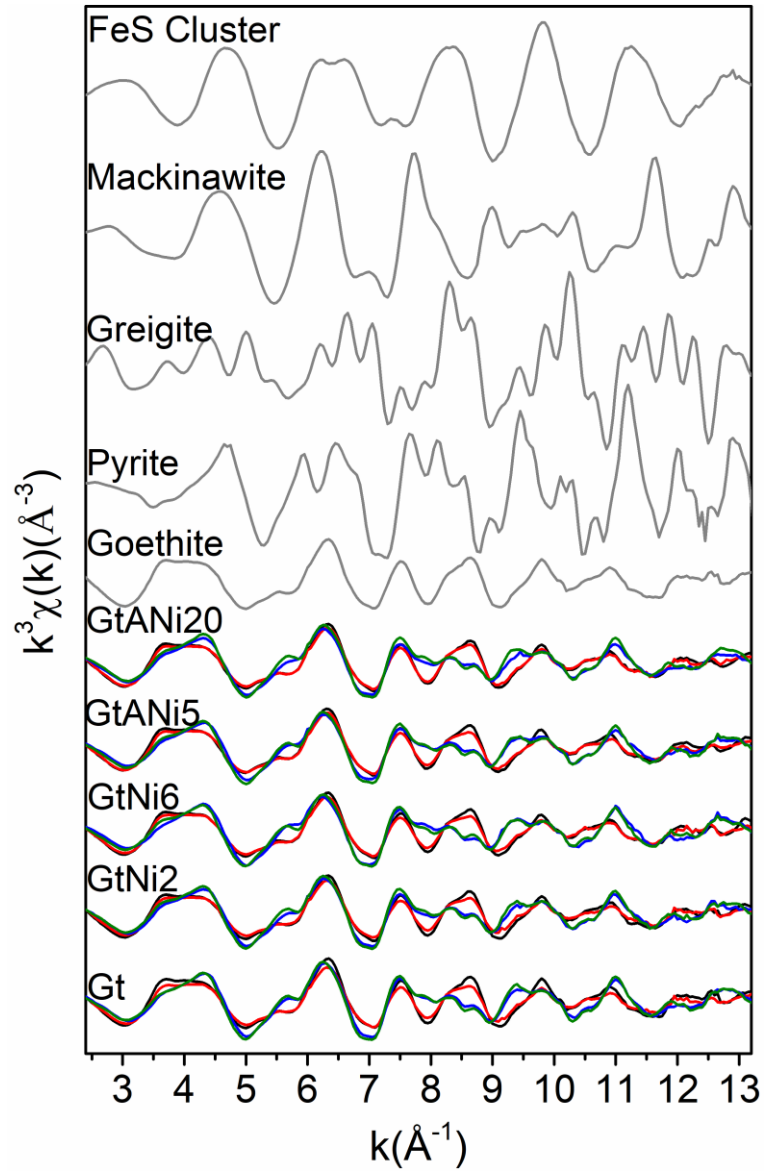


Fig. S2. Fe K-edge EXAFS spectra (k^3 weighted) obtained for pristine (black) and sulfidized goethite samples (red: 3 days, blue: 7 days, olive green: 44 days), and iron oxyhydroxide/sulfide standards (gray). Data for colloidal FeS from Noël et al. (2020). The Fe K-edge EXAFS spectrum of greigite was calculated with Feff8.4 (Ikogou et al., 2017) based on its structure model (COD#9000123).

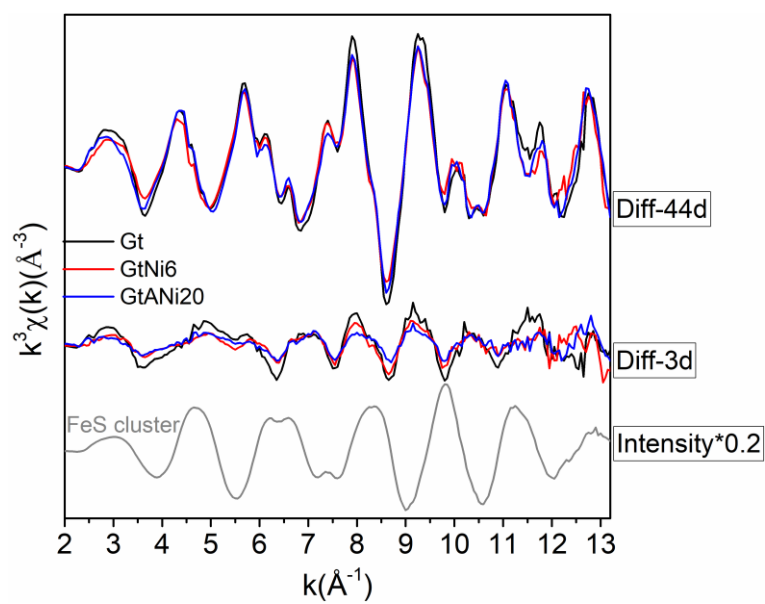


Fig. S3. Difference of Fe K-edge EXAFS spectra (k^3 weighted) between pristine and sulfidized samples (3 or 44 days of sulfidation) by comparison with a FeS cluster standard.

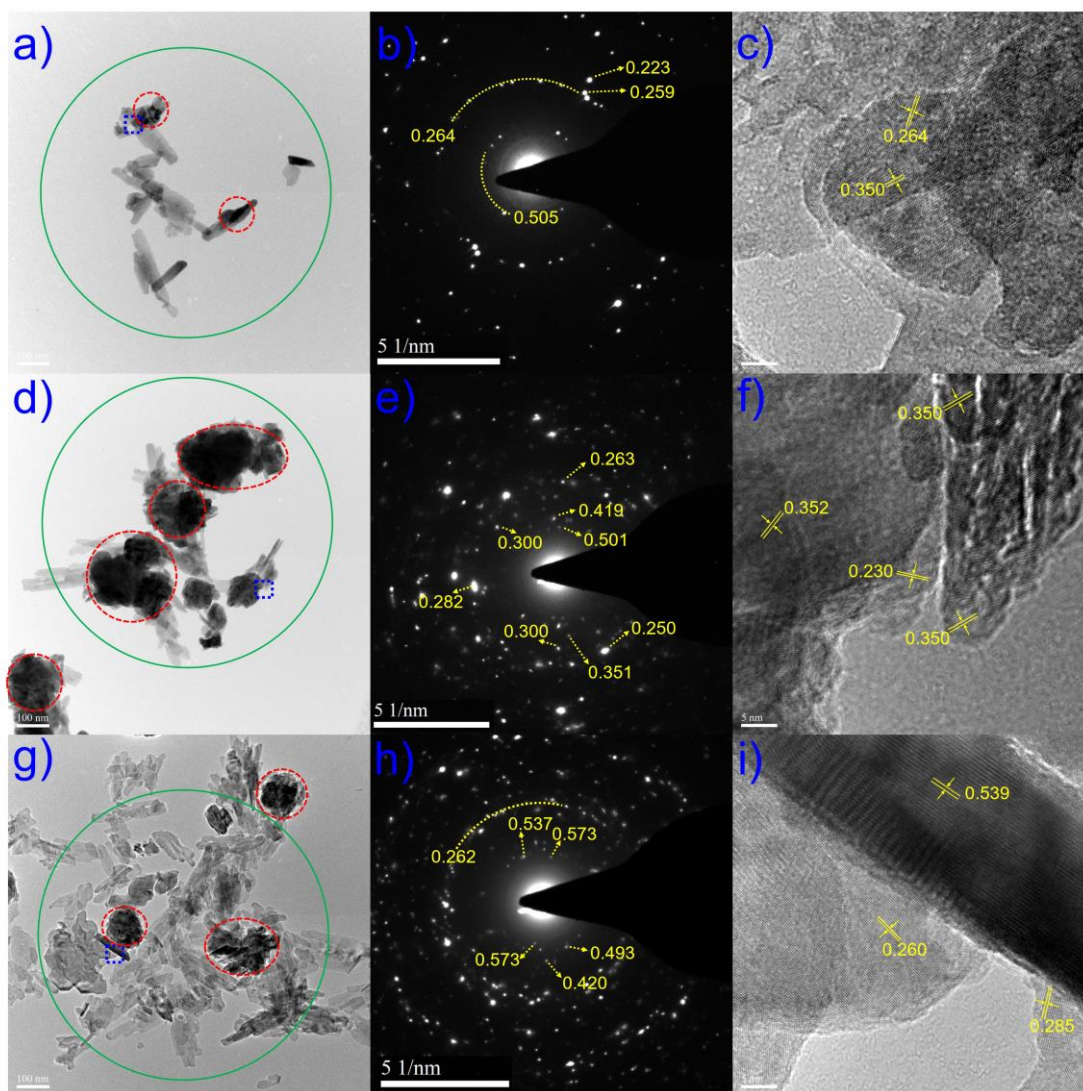


Fig. S4. Low magnification TEM images (scale bar is 100 nm) of samples sulfidized for 44 days: a): Gt-44d, d): GtNi6-44d, and g): GtANI20-44d. Those fibrous morphologies represent residual goethite crystals, and red dotted circles outlining polycrystalline aggregates indicate iron sulfides. b), e), and h): selected area electron diffraction (SAED) patterns of green circles indicated areas in a), d), and g), respectively. c), f), and i): high magnification images (scale bar is 5 nm) of the blue dotted rectangles shown in a), d), and g), respectively. Yellow values plotted on SAED patterns and lattice fringe images are distances (in nm). In particular, $\sim 0.282/0.285$, ~ 0.350 , and 0.573 nm correspond to (222), (220), and (111) of greigite (ICDD#16-0713) respectively, and that of $\sim 0.537/0.539$ nm are ascribed to (100) of pyrite (ICDD#42-1340), and ~ 0.300 nm indicates (311) of greigite or (101) of mackinawite (ICDD#15-0037). These numbers above couldn't be attributed to any plane of goethite (ICDD#29-0713).

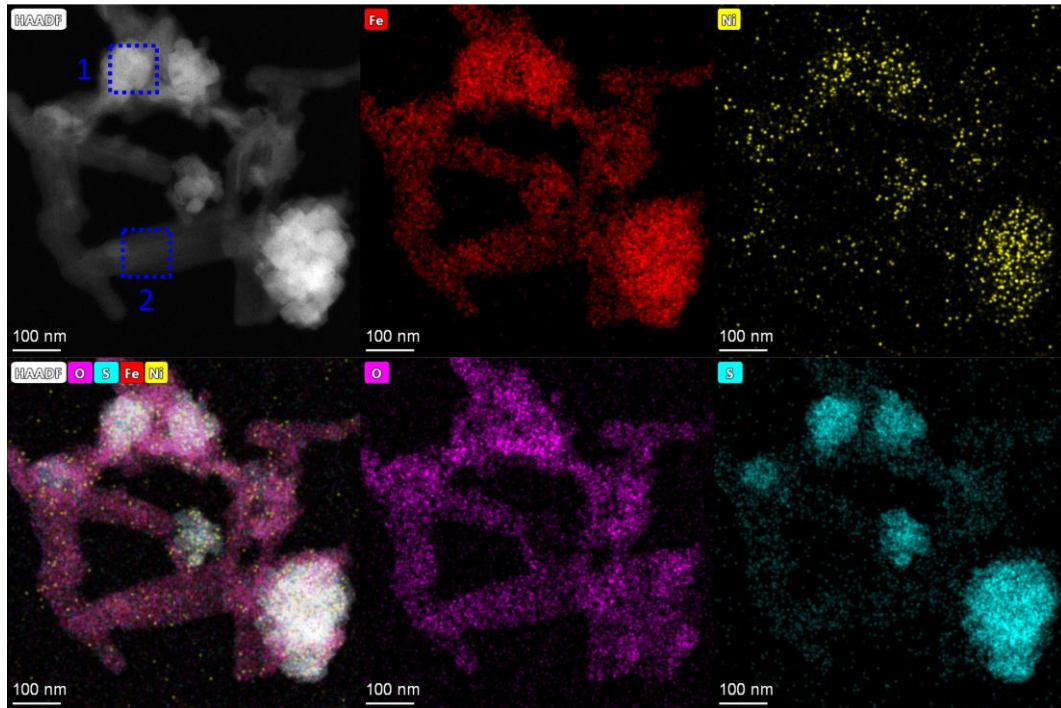


Fig. S5. STEM/HAADF micrograph (upper left) and EDX maps for Fe (upper center), Ni (upper right), O (lower center), S (lower right), and composite Fe-Ni-S-O obtained for GtNi6-44d. Ni mass fraction in area #1 (HAADF image) was $0.98 \pm 0.21\%$, that in area #2 was $0.82 \pm 0.50\%$.

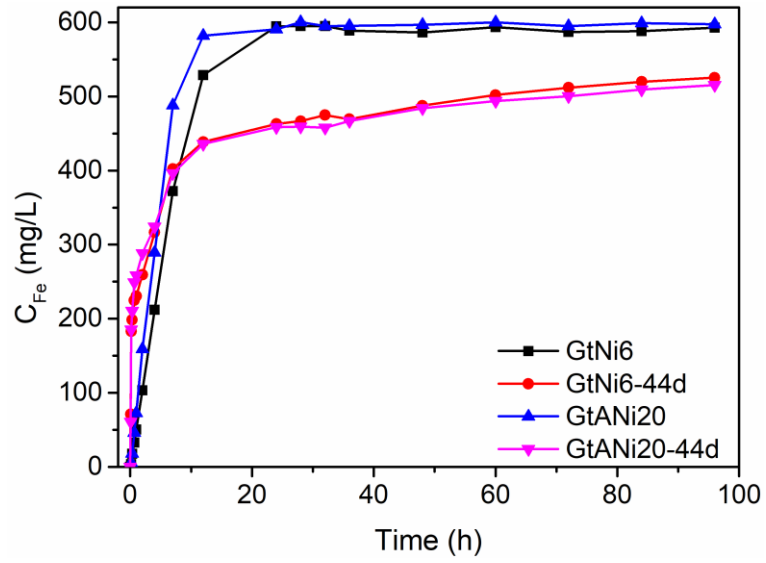


Fig. S6. Kinetic release of Fe (in concentration) during HCl treatment of pristine GtNi6 and GtANi20 and of their sulfidized counterparts. After 24 hrs, ~75% of Fe initially present in pristine goethites has been released from sulfidized samples.

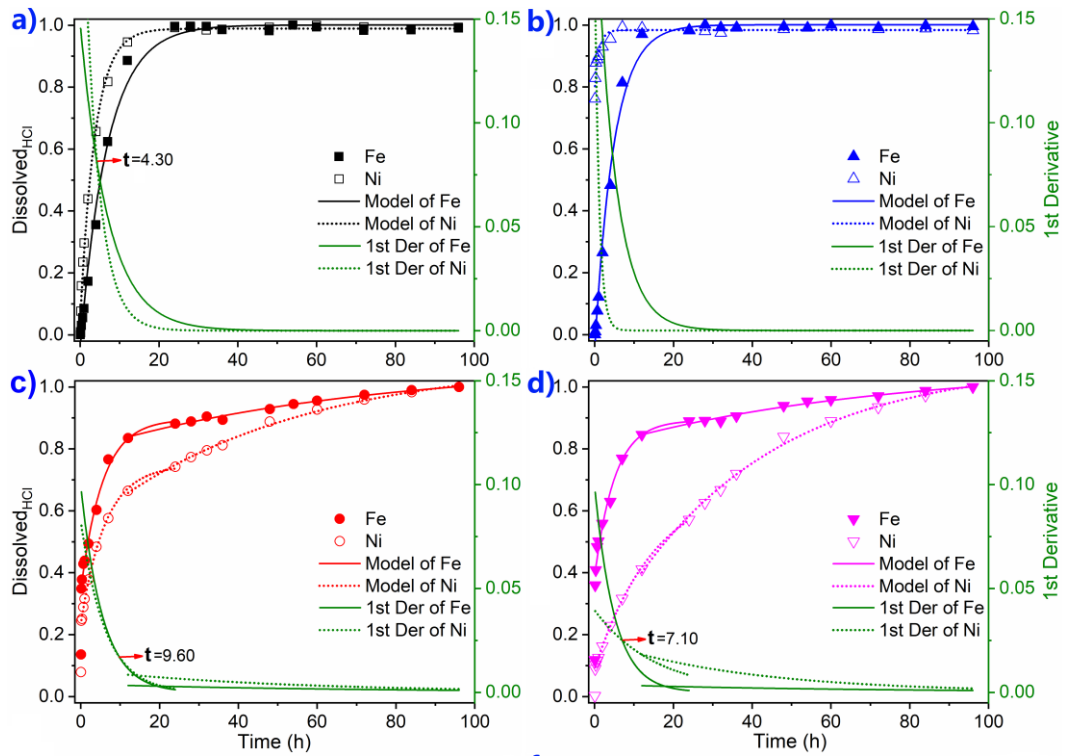


Fig. S7. Modeling of Fe and Ni kinetic release and corresponding 1st derivatives during HCl treatment of a) GtNi6, b) GtANi20, c) GtNi6-44d, and d) GtANi20-44d. Fits to the Fe and Ni data are shown as solid and dotted lines, respectively. 1st derivative curves are shown as green lines. Red arrows in a), c), and d) indicate the point where the 1st derivatives of Fe and Ni release are equal.

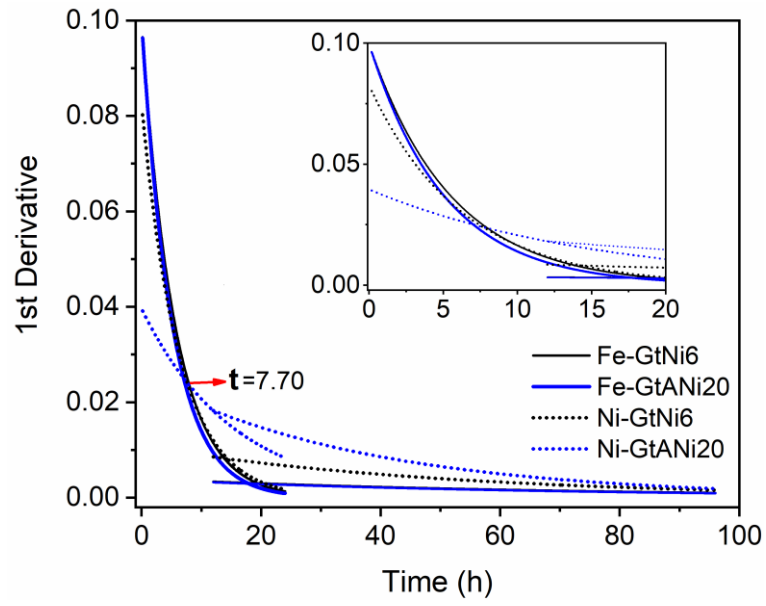


Fig. S8. First derivative of modeled Fe and Ni kinetic release of GtNi6 and GtANi20.

Table S1

Relative contents of Fe-bearing minerals determined from Rietveld refinement of XRD data in pristine Ni-free/-containing goethites and corresponding reaction products after interaction with S(-II).

Sample	Time	Goethite	Pyrite	Greigite	Mackinawite
		f%	f%/f _S %	f%/f _S %	f%/f _S %
Gt	0d	100	-/-	-/-	-/-
	3d	98.1	1.0(2)/-	0.1(1)/-	0.8(1)/-
	7d	61.7(5)	35.8(5)/93.7	0.6(2)/1.5	1.9(1)/4.8
	25d	59.5(5)	38.5(5)/95.1	1.1(2)/2.8	0.9(1)/2.1
	44d	41.5(5)	54.4(5)/92.8	2.8(2)/4.8	1.4(1)/2.4
GtNi2	0d	100	-/-	-/-	-/-
	3d	97.4	1.6(1)/-	0.2(1)/-	0.8(1)/-
	7d	70.9(5)	27.5(5)/94.6	0.4(1)/1.5	1.1(1)/3.9
	25d	57.8(6)	37.7(5)/89.4	3.3(2)/7.8	1.2(1)/2.8
	44d	54.1(5)	33.2(4)/72.4	9.7(3)/21.2	3.0(1)/6.5
GtNi6	0d	100	-/-	-/-	-/-
	3d	97.9	1.4(1)/-	-/-	0.7(1)/-
	7d	58.2(7)	39.1(6)/93.5	0.9(2)/2.2	1.8(1)/4.2
	25d	52.0(6)	33.9(5)/70.6	13.2(4)/27.4	1.0(1)/2.0
	44d	53.8(5)	33.5(5)/72.5	11.5(3)/24.8	1.3(1)/2.7
GtANi5	0d	100	-/-	-/-	-/-
	3d	97.8	1.6(1)/-	-/-	0.6(1)/-
	7d	66.0(6)	31.5(5)/92.5	0.8(2)/2.5	1.7(1)/5.0
	25d	57.3(6)	38.2(5)/89.5	3.0(2)/7.0	1.5(1)/3.6
	44d	50.4(6)	33.0(5)/66.6	11.0(3)/22.1	5.6(2)/11.2
GtANi20	0d	100	-/-	-/-	-/-
	3d	99.1	0.5(1)/-	0.3(1)/-	0.1(1)/-
	7d	69.1(5)	29.2(5)/94.6	0.4(2)/1.4	1.2(1)/4.0
	25d	48.5(8)	36.2(8)/70.3	13.9(8)/26.9	1.4(1)/2.8
	44d	47.6(5)	40.7(5)/77.7	3.7(2)/7.0	8.0(2)/15.3

Note: f% represents the mass fraction (wt.%) of a specific mineral in the samples, whereas f_S% represents the relative proportion of this mineral among iron sulfides (pyrite + greigite + mackinawite).

Table S2

Unit-cell parameters of Fe-bearing minerals in pristine Ni-free/-containing goethites and corresponding reaction products and fit quality parameters of the Rietveld refinement.

Sample	Time	Rwp	χ^2	Goethite			Pyrite	Greigite	Mackinawite	
				a	b	c	a	a	a	c
Gt	0d	2.05	1.27	4.629(5)	9.957(6)	3.025(2)	--	--	--	--
	3d	2.33	1.24	4.626(9)	9.958(10)	3.023(3)	5.435(12)	9.975	3.697(42)	5.083(66)
	7d	3.22	2.35	4.629(9)	9.964(12)	3.025(4)	5.427(5)	9.975	3.698(19)	5.083
	25d	3.75	1.42	4.630(12)	9.964(16)	3.025(5)	5.430(6)	9.922(47)	3.710	5.083
	44d	3.10	2.08	4.631(8)	9.963(11)	3.024(3)	5.429(4)	9.884(18)	3.662(23)	5.072(34)
GtNi2	0d	2.56	1.42	4.624(7)	9.966(8)	3.027(2)	--	--	--	--
	3d	2.49	1.21	4.619(8)	9.959(10)	3.022(3)	5.432(8)	9.953(28)	3.680(37)	5.083
	7d	3.00	1.98	4.620(10)	9.962(13)	3.023(4)	5.431(6)	9.975	3.704(27)	5.083
	25d	3.50	1.90	4.628(10)	9.968(13)	3.024(4)	5.433(5)	9.890(19)	3.672(31)	5.078(46)
	44d	2.90	2.06	4.622(7)	9.961(9)	3.023(2)	5.429(3)	9.872(17)	3.668(7)	5.050(15)
GtNi6	0d	2.22	1.31	4.624(5)	9.967(6)	3.026(2)	--	--	--	--
	3d	2.47	1.37	4.624(7)	9.965(9)	3.024(3)	5.435(8)	--	3.710	5.083
	7d	3.33	2.10	4.625(13)	9.975(18)	3.026(5)	5.439(6)	9.975	3.685(21)	5.083
	25d	2.88	1.90	4.621(8)	9.966(11)	3.022(3)	5.433(4)	9.875(17)	3.692(22)	5.083
	44d	2.70	1.70	4.622(7)	9.967(10)	3.023(3)	5.433(3)	9.879(14)	3.660(17)	5.063(26)
GtANi5	0d	2.08	1.17	4.629(4)	9.956(5)	3.025(1)	--	--	--	--
	3d	2.27	1.20	4.624(7)	9.955(9)	3.023(3)	5.425(7)	--	3.710	5.083
	7d	3.15	2.07	4.625(9)	9.961(12)	3.024(3)	5.433(6)	9.975	3.695(23)	5.083
	25d	3.13	1.76	4.630(9)	9.967(14)	3.025(3)	5.435(5)	9.907(20)	3.666(23)	5.083
	44d	2.79	1.67	4.624(8)	9.962(10)	3.023(3)	5.432(4)	9.877(13)	3.670(5)	5.045(10)
GtANi20	0d	2.12	1.23	4.629(4)	9.956(5)	3.025(1)	--	--	--	--
	3d	2.13	1.11	4.626(7)	9.960(8)	3.025(2)	5.440(14)	9.783(110)	3.710	5.083
	7d	2.96	1.95	4.628(10)	9.968(13)	3.026(4)	5.439(6)	9.975	3.710	5.083
	25d	3.18	1.95	4.633(10)	9.965(15)	3.025(4)	5.438(5)	9.887(76)	3.683(23)	5.049(36)
	44d	3.15	1.84	4.624(8)	9.960(11)	3.023(3)	5.432(4)	9.883(14)	3.672(4)	5.047(10)

Table S3

Kinetic parameters computed for Fe (y_1) and Ni (y_2) release from solids in HCl solutions.

Acid Treatment	HCl	
Time	0.167-24 h	24-96 h
GtNi6	$y_1 = -1.04 * e^{-t/7.02} + 1.00, r^2 = 0.9957;$ $y_2 = -0.94 * e^{-t/3.75} + 0.99, r^2 = 0.9970;$	
GtANi20	$y_1 = -1.05 * e^{-t/4.90} + 1.00, r^2 = 0.9955;$ $y_2 = -0.20 * e^{-t/1.09} + 0.98, r^2 = 0.9346;$	
GtNi6-44d	$y_1 = -0.55 * e^{-t/5.55} + 0.90, r^2 = 0.9932;$ $y_2 = -0.51 * e^{-t/6.22} + 0.75, r^2 = 0.9989;$	$y_1 = -0.28 * e^{-t/69.25} + 1.07, r^2 = 0.9888;$ $y_2 = -0.55 * e^{-t/45.94} + 1.07, r^2 = 0.9903;$
GtANi20-44d	$y_1 = -0.51 * e^{-t/5.09} + 0.89, r^2 = 0.9832;$ $y_2 = -0.61 * e^{-t/15.41} + 0.70, r^2 = 0.9993;$	$y_1 = -0.26 * e^{-t/67.69} + 1.06, r^2 = 0.9956;$ $y_2 = -0.93 * e^{-t/37.01} + 1.07, r^2 = 0.9956;$

References:

- Ikogou M., Ona-Nguema G., Juillot F., Le Pape P., Menguy N., Richeux N., Guigner J. M., Noel V., Brest J., Baptiste B. and Morin G. (2017) Long-term sequestration of nickel in mackinawite formed by *Desulfovibrio capillatus* upon Fe(III)-citrate reduction in the presence of thiosulfate. *Appl. Geochem.* **80**, 143-154.
- Nöel V., Kumar N., Boye K., Barragan L., Lezama-Pacheco J. S., Chu R., Tolic N., Brown G. E. and Bargar J. R. (2020) FeS colloids - formation and mobilization pathways in natural waters. *Environ. Sci. Nano* **7**, 2102-2116.